

Dashtkar, Arash, Hadavinia, Homayoun, Sahinkaya, M Necip, Williams, Neil, Vahid, Samireh, Ismail, Fanya and Turner, Matthew (2019) Rain erosion-resistant coatings for wind turbine blades : a review. *Polymers and Polymer Composites*, 27(8), pp. 443-475. Copyright © 2019 (The Authors).
DOI: <https://doi.org/10.1177/0967391119848232>

Rain erosion resistant coatings for wind turbine blades – A review

Arash Dashtkar^a, Homayoun Hadavinia^{a,1}, M. Necip Sahinkaya^a, Neil A. Williams^b, Samireh Vahid^a, Fanya Ismail^c, Matthew Turner^d

^a School of Engineering & Environment, Kingston University London, UK

^b School of Life Sciences, Pharmacy and Chemistry, Kingston University London, UK

^c LYN Coatings Ltd, 8 Pier Road Industrial Estate, Pier Approach Road, Gillingham, ME7 1RZ, UK

^d Haydale Composite Solutions Ltd, Unit 10 Charnwood Business Park, North Road, Loughborough, Leicestershire LE11 1QJ

Abstract

Wind blades are the most expensive parts of wind turbines made from fibre reinforced polymer (FRP) composites. The blades play a critical role on the energy production, but they are prone to damage like any other composite components. Leading Edge (LE) erosion of the wind turbine blades is one of the common damage, causing a reduction in the Annual Energy Production (AEP) especially in offshore wind turbine farms. This erosion can be caused by rain, sand and flying solid particles. Coating the blade against erosion using appropriate materials can drastically reduce these losses and hence is of great interest. The sol-gel technique is a convenient method to manufacture thin film coatings, which can protect the blades against the rain erosion, while having negligible effect on the weight of the blades. This paper provides an extensive review of the liquid erosion mechanism, water erosion testing procedures and the contributing factors to the erosion of the LE of wind turbine blades. Techniques for improving the erosion resistance of the LE using carbon nanotubes (CNTs) and graphene nano-additives are also discussed.

Keywords: Erosion; Turbine blade; Sol-gel; Water impingement; Rain impact; Water impact

¹ Corresponding authors: T: +44 208417 4864; E: h.hadavinia@kingston.ac.uk (H. Hadavinia)

Table of Contents

Abstract	1
1. Introduction	2
2. Erosion of the wind turbine blade	4
2.1. Liquid erosion parameters	7
2.2. Liquid erosion mechanism of the blades	8
2.3. Evaluation of erosion damage.....	11
2.4. Erosion prevention systems	11
2.5. Coating of the wind turbine blades.....	12
2.6. Design of liquid impact testing apparatus.....	12
3. The sol-gel technique	17
3.1. Advantages of sol- gel technique over traditional techniques.....	19
3.2. Sol-gel process.....	20
3.3. Techniques for deposition of sol-gel coatings.....	20
3.4. Sol-gel applications.....	23
3.5. Evaluation of mechanical properties of sol-gel derived coatings.....	24
3.6. Sol-gel fast curing	27
4. Sol-gel with additive carbon nanotubes and graphene nanoparticles	28
4.1. Carbon nanoparticles (CNPs)	29
4.2. Increasing hardness of sol-gel coating	38
4.3. Increasing the resilience of the sol-gel coating	42
4.4. Increasing the adhesion of the sol-gel coating to the substrate	43
4.5. Increasing the water contact angle in sol-gel coating	45
5. Conclusion.....	46
5.1. Prospect of new development of erosion resistance coating.....	47
References	48

1. Introduction

Global energy demand is continually rising due to an increasing population and industrialisation and increasing dependence on electric and electronic devices. According to the British Petroleum (BP) energy outlook 2017, the population of the world will be nearly 8.8 billion by 2035. The increasing global energy demand and the limited fossil fuels resources and environmental concerns make the expansion of renewable energy resources essential in order to supply the demand. Hydropower, wind turbines and solar power are the top three sources of renewable energy [1].

A wind turbine is a machine that converts the kinetic energy of the wind into mechanical energy and then by the help of a generator converts this mechanical energy into electricity. The performance of the wind turbine is dependent on the appropriate design of blades and the endurance of the blade shape and geometrical dimensions during its lifespan [2] hence attention to the structural health of the blades is important in the design phase. Poor erosion-resistance of blade materials will result in sub-optimal operation of the blade and may also compromise the structural integrity of the blade. A consistent erosive pattern has been reported that consists of four phases: Upper core breach, lower core breach, leading edge core breach and advanced erosion [3]. Most of the structural damage of the wind turbine was found in the blades and tower of the turbine [4]. It is reported that 15% to 20% of the total turbine cost is on the manufacture and installation of the blades [4]. Repairing the blades is the most expensive and most time consuming process in the maintenance of

wind turbines [5]. Currently there are two general surface coating systems that are commonly used by wind turbine manufacturers. One group called “gelcoat” either applied in mould during the manufacturing process (polyester based) or painted on the blade (epoxy based). The second group is polyurethane based surface coating/paint which can be applied to the surface by spraying. The polyurethane coatings are highly elastic and durable material that act as an energy absorber at impacts, have shape memory as a result of high elasticity, resistant to gouging and abrasion [6]. These coatings serve to protect the underlying composite laminates from weathering and foreign object impact [7].

There are two main aerodynamic forces at work in wind turbine blades, lift and drag forces [8]. A suitable blade is designed to have a maximum lift to drag ratio, which is called glide ratio. The blades of wind turbines are cantilever beams up to 100m in length. As a result, the weight of the blade is one of the most important factors in the selection of the materials for the blade. Different parts of the blade are subjected to compression load, tension load or a combination of compression and tension. Materials should be chosen in a way to maintain the defined shape of the blade under various loads during its operation; they must be strong enough to resist the extreme loads, sufficiently stiff avoid buckling and to prevent collision with the tower under extreme loads and also the materials need to last the expected life (20-30 years) of the turbine under fatigue loading [9, 10]. Fibre reinforced polymer (FRP) composites are used typically to manufacture the blades and the nacelle of the turbines while the generator and tower are manufactured from metals as they have all characteristics to meet these requirements. Currently the most used FRP composites in the structures of wind turbine blades are glass fibre (GFRP) and carbon fibre (CFRP) composites. Glass fibres have good specific strength, low specific stiffness and are inexpensive while, carbon fibres have high specific strength and are about five times stiffer than GFRP but they are more expensive. Using CFRP reduces the tip deflection of the blades and allows the manufacturer to make longer blades, but the cost is much higher [11]. Recently research showed that hybrid carbon/glass composites represent an interesting alternative to the pure GFRP or CFRP materials. Hybrid composites has been used in the manufacturing of LM Wind Power 84.4m wind turbine blade [12] which has a blade mass of 34 t and a rated tip speed of 80m/s. The trend of increasing the rotor diameter is continuing in the future resulting in higher tip speed. When considering the impact of rain droplets, the tip speed is a key contributor to erosion damage. The erosion of the blade will cause turbulence, and lead to a decrease in lift and an increase in the drag forces. It was shown that drag could be increased from 6% to 500% depending on the degree of leading edge erosion [13, 14]; increasing the drag by 80% will reduce the annual energy production of the wind turbine by 5% [15]. Excessive damage could lead to total failure of the blade. This is more significant for offshore wind turbines with larger blades and higher tip speeds than onshore turbines [16]. As a result, development of erosion resistant coatings for protection of the blades is very important, for both Levelised Energy Cost (LEC) and maintenance of the structural integrity of the blade to avoid weight unbalancing.

There is no comprehensive review in the literature on LE erosion protection using sol-gel technique. In this paper the state-of-the-art erosion resistance coatings for wind turbine blade is reported. Various tests methods and apparatus developed by different researchers for accelerated testing of the coated blades materials under water impact condition are presented. The use of carbon nanoparticles (CNP) for improving the erosion resistance of sol-gel coating is discussed.

2. Erosion of the wind turbine blade

Erosion has been reported after two years of operations in some wind turbine blades [17, 18]. Inspection of 201 blades in 67 wind turbines operated by EDP Company showed that erosion occurred at the leading edge of 174 blades, which is around 87% of inspected blades [14]. Modern and large wind turbines are affected less by particle erosion in comparison with the small turbines. The reason may be the increased influence of the blade flow field towards a deviation of the incoming particles [3]. It was noted that offshore wind farms are subjected to more intense particle erosion than the majority of in land installations. The main causes of blade damage were identified as sand grains and raindrops, other impactors such as insects and hailstones do not have a significant effect on the erosion of wind turbine blade [3]. LE erosion causes an increase in surface roughness of the blade and thereby an increase in the air flow boundary layer thickness over the aerofoils on the blade when it is operating. The increased boundary layer thickness causes an increased drag coefficient and a decreased lift coefficient, and thus reduces the aerodynamic performance, particularly at higher angles of attack [15]. The consequence is severe losses in energy production. It has been reported that eroded blades in wind turbine can reduce Annual Energy Production (AEP) by as much as 20% to 25%, [13, 19]. Coating the blade against erosion using appropriate materials can drastically reduce these losses and hence is of great interest.

Due to the impact of erosion on the operation of wind turbine blades they need to be monitored during their lifespan, however, the health monitoring process of a blade surface is time consuming and costly [20]. During the monitoring process, wind farm need to be shut down and then photographed from the ground. The location, depth and roughness of the damaged areas are the main aspects that are monitored as they affect the aerodynamic performance of the blade.

Liquid impingement erosion is important primarily where the target body moves at high speeds and collides with liquid drops that are moving much slower as is the case for wind turbine blades. Due to the higher blade speed at the outer part of the blades, erosion mostly appears at the LE in this area (**Figure 1**). For this reason maintenance of the leading edge of the blade is not only recommended but it is essential if blades are expected to reach their life expectancy.

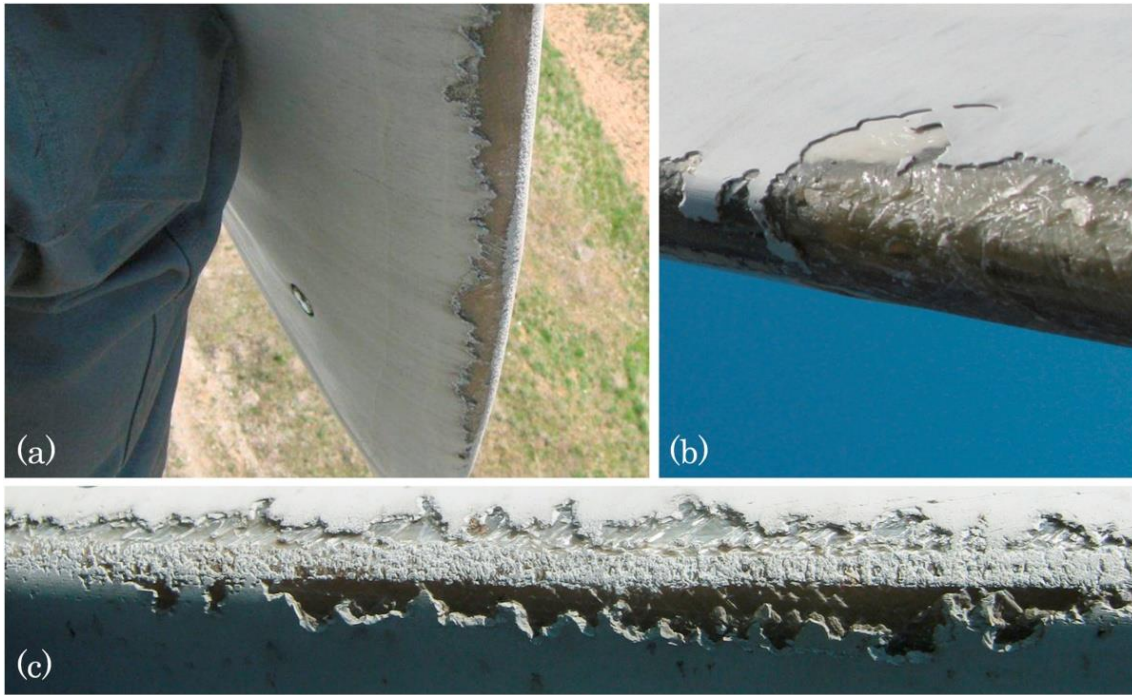


Figure 1. (a) Eroded wind turbine blade tip [21], (b) detail of eroded LE [22] and (c) close-up of eroded LE [21]. Reprinted from Ref. [23] with the permission of Elsevier Publishing. Reprinted from O’Carroll et al. [22] with the permission of Elsevier publishing. LE: leading edge.

Leading edge erosion of the wind turbine blades can cause water ingress, with water entering the blades through surface defects due to erosion resulting in degradation to the constituent components of the blades. Water absorption by the resin will increase the weight of the composite structure causing imbalances and an increase in wind turbine vibrations [24]. In some studies instead of water, rubber balls are used to impact specimen surfaces [25, 26].

The erosive force of rainfall is expressed as rainfall erosivity [27]. Rainfall erosivity considers the rainfall amount and intensity, and is most commonly expressed as the R-factor in the Universal Soil Loss Equation (USLE) model and its revised version (RUSLE). Estimation of the potential erosion caused by rain at specific wind farm sites is more challenging at sea than at land due to the limited available precipitation data. Over land, the rainfall erosivity for soil degradation has been assessed from 1541 precipitation stations in all European Union (EU) Member States and Switzerland, with temporal resolutions of 5 to 60 min [27, 28]. The map on rainfall erosivity in Europe at 500m spatial resolution assessed by European Soil Data Centre (ESDAC) is shown in Fig. 11 [27]. This database is valuable for the production of a rain erosion map for wind turbines where precipitation, wind speed and turbine characteristics such as tip speed would be input [29].

In order to understand the details of erosion process and characterise the failure mechanism, numerical models of rain droplet impact simulations are necessary [30, 31].

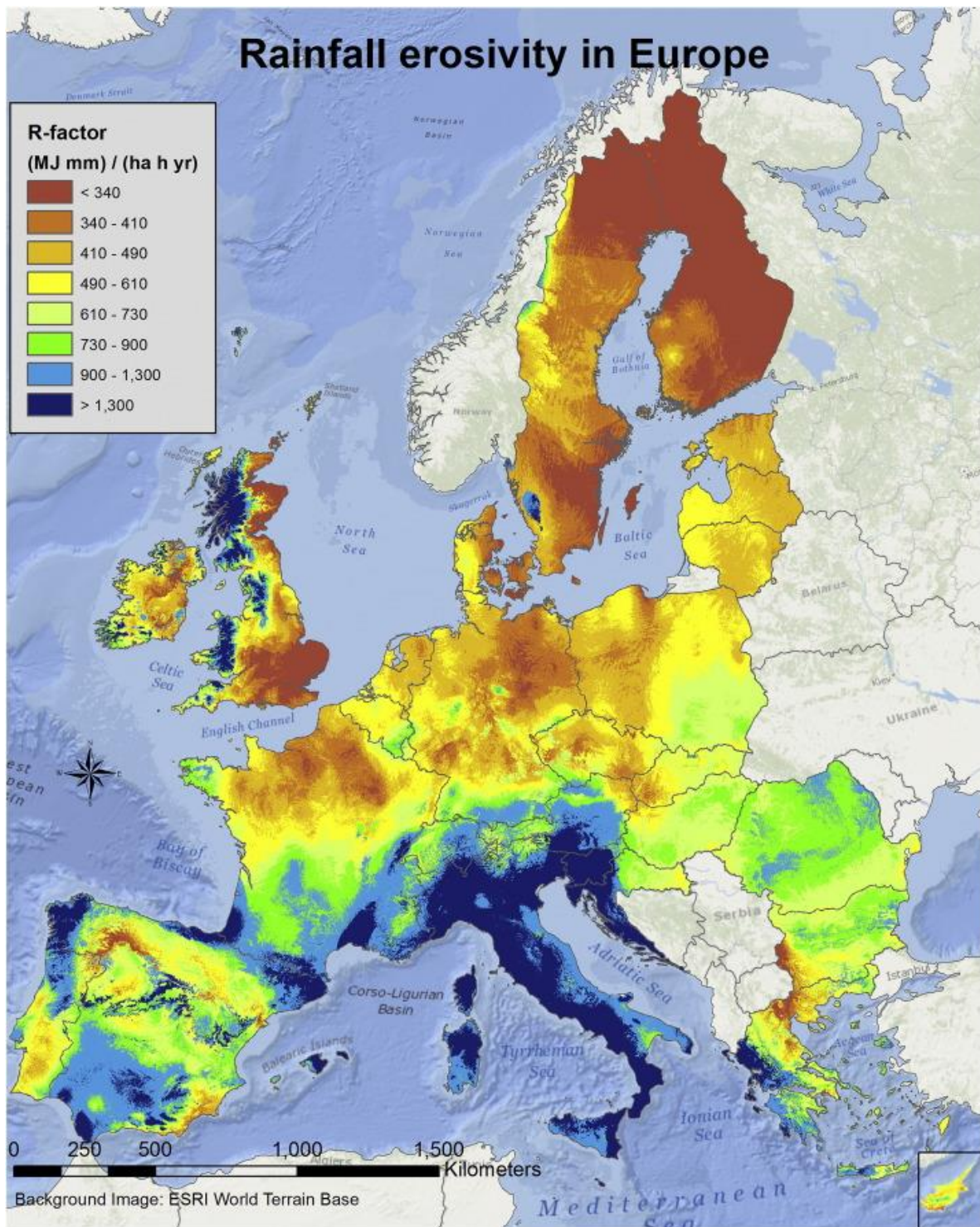


Figure 2. Rainfall erosivity in Europe at 1 km grid cell resolution. Reprinted from Ref. [27] with the permission of Elsevier Publishing.

2.1. Liquid erosion parameters

There are a number of parameters that affect erosion by liquid droplets. These parameters are: speed of impact, impact angle, droplet size, liquid density, acoustic velocity, cyclic properties of materials, hardness and geometrical aspects.

Impact speed. To explain the relationship between the erosion rate and impact speed, equation (1) can be used.

$$V_m = cV^4d^3n_m \quad (1)$$

Where, V_m is erosion rate and (c) is a constant. The erosion rate V_m can be evaluated from equation (1) by using the experimental data of the droplet velocity V , the droplet diameter (d) and the number of impinging droplets n_m [32]. The droplet velocity can be measured by particle image velocimetry, its diameter by shadowgraph technique and the number of impinging droplets in a unit area can be counted by a sampling probe [32, 33, 34].

Recently, the influence of the liquid film on the erosion rate is found to be the other influential droplet parameter. The thickness of the liquid film is an important factor for quantitative prediction of erosion rate [35, 34]. Generally, the erosion rate is directly proportional to the droplet size [36]. Different sizes of droplet cause different erosion damage, the difference is more significant for lower velocities. To analyse the effect of the droplet size on the erosion phenomena, two aspects should be considered. First the same volume of water should impinge the samples and second samples should be tested at speeds higher than the threshold speed to damage. Although droplet size and shape has an effect on the impact velocity, impact pressure is independent of the droplet size or shape [36]. Increasing the impact frequency of the water droplet also increases the damage depth rate and decreases the incubation period [37].

Impact angle: Impact angle is the angle between the direction of the water motion and the target surface [38]. The effect of the impact angle can be neglected if the incubation period for crack formation is short enough [39]; but if the incubation period is not short enough, the amount of volume loss will be different for different impact angles and the highest volume loss will be at a 90° angle of attack.

Initial surface condition: A slightly roughened surface will erode faster than a smooth surface. So the constant rate of erosion at the terminal stage for rougher surface can be realized in a shorter time period than for a smooth surface [40, 34].

Mechanical properties of the surface: Although hardness is the most common property that determines erosion damage, yield strength, modulus of elasticity, wear resistance, ultimate rebound resilience, and fracture toughness are the other factors that have an influence on erosion damage.

Temperature: Both the environmental temperature and liquid drop temperature have an effect on the erosion damage. The erosion rate will increase at higher temperatures due to the reduction in the viscosity of the liquid.

2.2. Liquid erosion mechanism of the blades

Failure due to liquid impact of water droplets which causes damage in the form of pitting or peeling over time is divided into two regimes.

Water droplet inlet: When the contact edge travels across the surface of the target at a velocity (V_c) greater than the velocity of shock wave (C) propagating into the water drop, the initial damage occurs (

Figure 3). This damage happens because of the water hammer pressure which can be up to several MPa. This pressure can introduce initial cracks in the coating which can lead to the second stage of erosion mechanism (shear stress) [41].

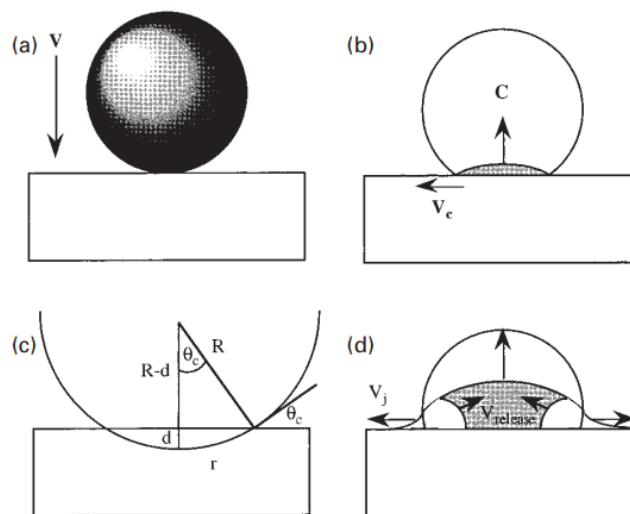


Figure 3. Sequence of liquid impact from initial impact through to release of high pressure: (a) at impact; (b) where water drop is compressed due to lack of free surface; (c) at release; (d) after shock wave has overtaken contact edge allowing decompression and jetting; dark regions in (b) and (d) represent area of compressed fluid. Reprinted from Jackson and Field [42].

To calculate the shock wave velocity into the water drop, the following equation can be used for impact velocity up to 1000m/s:

$$C = C_0 + kV \quad (2)$$

where C_0 is acoustic velocity, V is the droplet impact velocity and value for k is approximately 2.

Lateral jets: After the first stage, the water trapped in the compressed region can escape and generate water flow across the surface producing a high velocity sideways jet of fluid [42]. The velocity of the lateral jet is greater than the impact velocity and can cause material loss and extension of cracks (Figure 4).

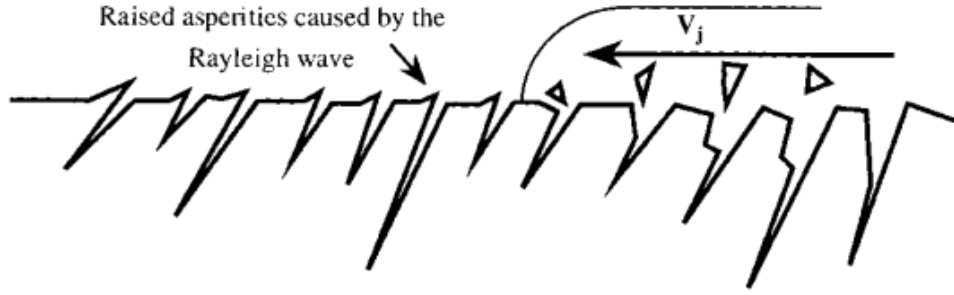


Figure 4. Damaging effects of lateral jetting; left hand side damaged by Rayleigh wave only; as lateral jetting crosses surface it tears off asperities it collides with. Reprinted from Jackson and Field [41].

Droplet after shockwave overtakes contact edge and generates a free surface which allows the compressed region to be released. From this free surface, three types of waves propagate into the water droplet to reduce the water hammer pressure. This incompressible pressure can be calculated by following equation [43]:

$$P_w = \rho CV = \rho \left(1 + k \frac{v}{c_0} \right) \quad (3)$$

where ρ is the water density 1000 kg/m^3 , C is the shock wave velocity and v is the droplet impact velocity as before. As an example, water impacting at 500 m/s gives an impact pressure of about 1250 MPa . The stagnation pressure of continuous jet acting at this speed calculated from $\rho V^2/2$ is about one tenth of this value [36].

Compression, shear and Rayleigh are the three stress waves, which play critical roles in the erosion process (Figure 5). The compression wave is the fastest one, whereas the shear wave is slower. The compression wave has small effect on causing the damage. The Rayleigh wave is the one, which interacts with the surface cracks. This wave has both vertical and horizontal components. The vertical component penetrates into the depth of the surface and it depends on the impact velocity and radius of the drop. The total impact energy, divided between these three waves is: Rayleigh wave (67.4%), shear wave (25.8%) and compression wave (6.9%). Stress reflections oscillate repeatedly through the coating and substrate structure until they dampen out and the energy of the initial shockwave is reduced [44].

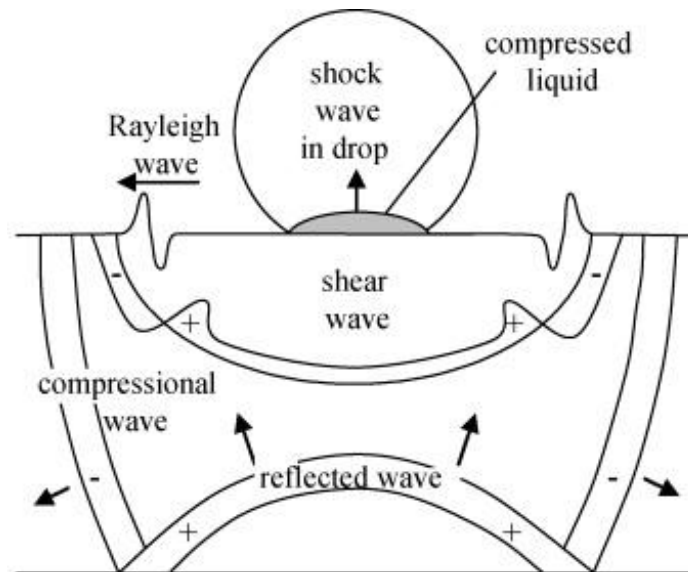


Figure 5. Three types of stress waves generated in isotropic brittle solid. Reprinted from Zahavi and Nativ [44] with the permission of Elsevier Publishing.

Spalling and lateral delamination between two coatings can be expected because of mismatch of the physical properties of both materials. In another word when an elastic wave reaches a free surface or interface between solids having different physical properties, the resultant wave can cause material failure [45, 44].

The process of liquid erosion occurs in the following stages:

- Incubation stage, where the surface remains unaffected and there is no record of significant mass loss (Figure 6). This stage may not appear if the impact conditions are severe enough to cause material loss for a single impact.
- Acceleration stage; during which rate increases rapidly to a maximum
- Maximum rate stage; where the erosion rate remains (nearly) constant
- Deceleration (or attenuation) stage; where the erosion rate declines to (normally) 1/4 to 1/2 of the maximum rate
- Terminal (or final steady-state) stage; in which the rate remains constant once again indefinitely. However, in some cases the erosion rate can continue to decline or fluctuate. Also, for some brittle materials, the rate can increase once again in what is called a “catastrophic stage” [36].

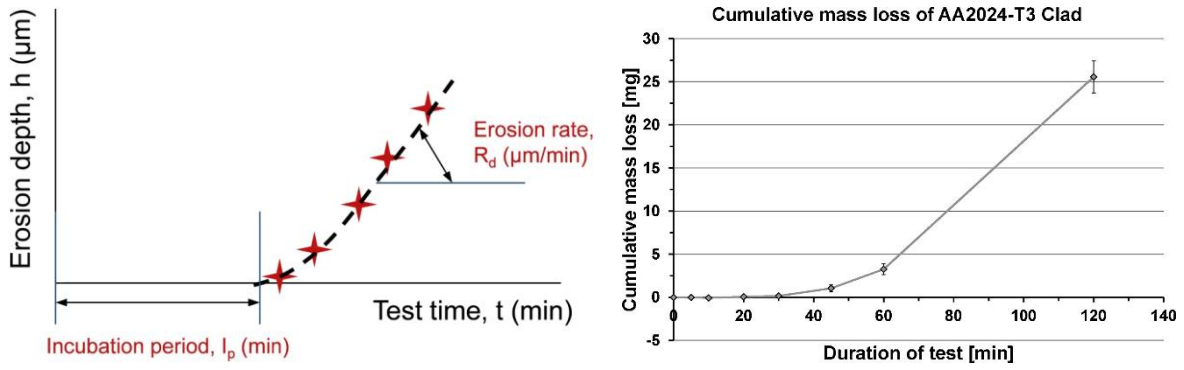


Figure 6. The incubation period and the stage with a constant erosion rate [46] (right), cumulative mass loss [47] (left)

Generally surface erosion in the turbine blade gradually expanded from the pressure side near the stagnation point to the suction side and the depth and width of the erosion increases in section closer to the tip [14].

2.3. Evaluation of erosion damage

Damage caused by rain erosion can be evaluated by analysing the erosion depth and incubation period.

Erosion depth. It is the local volume of damage per small area and it can be calculated by equation (4)

$$E_d = R_d (t - I_p) \quad (4)$$

Where E_d is damage depth in (mm), R_d is damage depth rate in (mm/s), t is the time and I_p is the incubation period in second [34].

Incubation period: all the materials exhibit an incubation period where no damage is observed up to a certain level of exposure to rain impact, but beyond this period of exposure, erosion damage increases rapidly [48, 43]. The amount of erosion damage per unit mass of droplets can be calculated by using the following equation:

$$E = \frac{R_d}{F_{req} \cdot \rho \left(\pi \cdot \frac{D^3}{6} \right)} \quad (5)$$

Where E is the erosion damage per unit mass of droplets ($\text{mm}^3 \text{kg}^{-1}$), R_d is damage depth rate in (mm/s), F_{req} is the impact frequency of the water droplet (number $\text{mm}^2 \text{s}^{-1}$) and D is the diameter of the water droplet [37].

2.4. Erosion prevention systems

Erosion by liquid impingement can be reduced by a Lower impact velocity, a decrease in normal component of the velocity (e.g. “tilting” the surface), smaller droplet size, shorter operation times under severe conditions, more resistant materials and the application of a shielding layer.

The most effective system to protect the wind turbine blades against the erosion is using an erosion resistant coating. There are two common techniques to produce an effective surface coating, in-mould application and post-mould application. For the in-mould application, a surface coating layer of material similar to the matrix material is added to the surface of the blade as part of the moulding process. In the case of post-mould application, a surface coating is applied after the moulding process by different methods of coating [11]. It should be kept in mind that using the coating to protect the leading edge of the blades from the rain erosion will change the shape of the initial aerofoil section slightly which can have effect on the aerodynamic performance of the turbine; but this effect is negligible in comparison with the effects of the eroded blade on the performance of the turbine [13, 49].

2.5. Coating of the wind turbine blades

Materials are coated for a number of reasons such as to: make a substrate biocompatible, increase a material's thermal, mechanical or chemical stability, increase the wear resistance, improve the durability, decrease friction, inhibit corrosion or change the overall physicochemical and biological properties of the material [50]. As they are the most sensitive area of the wind turbine, Protective layers such as tape or paintable and elastic coating are used for mitigating leading edge erosion of the blades. These layers absorb the impact energy without crack formation. The ability of a coating to absorb and distribute the energy from an impact can vary and this is expressed by the impact frequency [17]. Current blade coating systems typically consist of a putty layer which is applied for filling pores in the composite substrate, a primer to secure good adhesion of the subsequent coat and a flexible topcoat usually from a polyurethane-based formulation [17]. If leading edge protection has not been applied during the manufacturing process, leading edge erosion can occur within two years of operation. A rough estimation suggests 50% of new large wind turbines are specified with a blade coating [20]. There is a variety of procedures for coating including: vapour deposition, chemical milling, layer-by-layer coating, dip coating and sol-gel coating technique [50]. The development of new coatings, which can protect the leading edge of the blades against the erosion, is a topic of current research. Super hydrophobic coating using nanoparticles embedded in a resin [51], hydrophobic coating with anti-icing capability [52] and ceramic coating materials with a high-erosion resistance [18] are some of these coating which are used in the industry to protect the leading edge of the wind turbine blades.

2.6. Design of liquid impact testing apparatus

There are two methods for performing accelerated rain erosion tests; one method uses a whirling arm, which carries the specimens and rotates them under an artificial rain field produced by nozzles or needles [47] and in the other method a high velocity stream or jet of water is fired onto a stationary test specimen [53, 54]. The two methods are generally similar, one of the differences between these methods is the active/passive impact mode between water droplets/jet and test specimens [17] and another difference is that the

continuous jet produces stagnation pressure, whereas the discrete impacts in liquid droplet impingement produce much larger shockwave pressures.

2.6.1. Critical parameters for design

Stand-off Distance (SOD): The distance between the nozzle and the specimen surface has a significant effect on the erosion rate (See Figure 7).

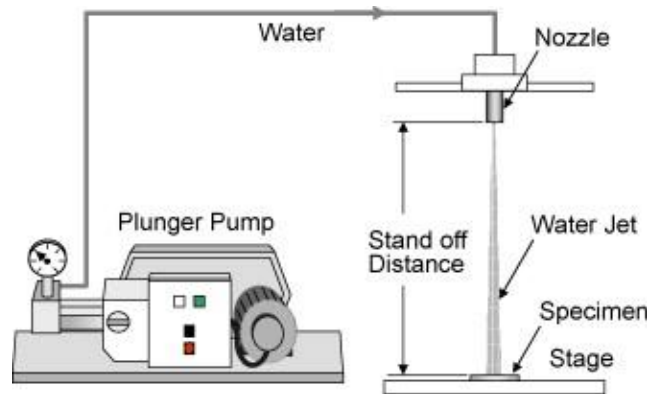


Figure 7. Schematic illustration of a testing apparatus. Reprinted from Oka and Miyata [18] with the permission of Elsevier Publishing.

The damage depth rate will decrease for very short or very long SOD. If the distance is too short (less than the intact length), it will cause negligible material removal because, in the short SOD the water that hits the surface forms a water column instead of water droplet. It is known that water droplet impact is more damaging than the impact of an intact fluid stream [38, 45, 55]. Intact length is the minimum distance from the nozzle over which the liquid jet is still connected [56, 57, 58]. The effect of the SOD on the erosion volume can be explained in four steps. As can be seen in Figure 8, erosion starts immediately after the incubation period and is then followed by the acceleration, maximum rate, deceleration and terminal erosion stages [36]. The decrease of the erosion rate far from the nozzle can be explained by the decrease in the droplet velocity; however, the decreased erosion rate in the near field is because of the influence of the liquid film over the specimen.

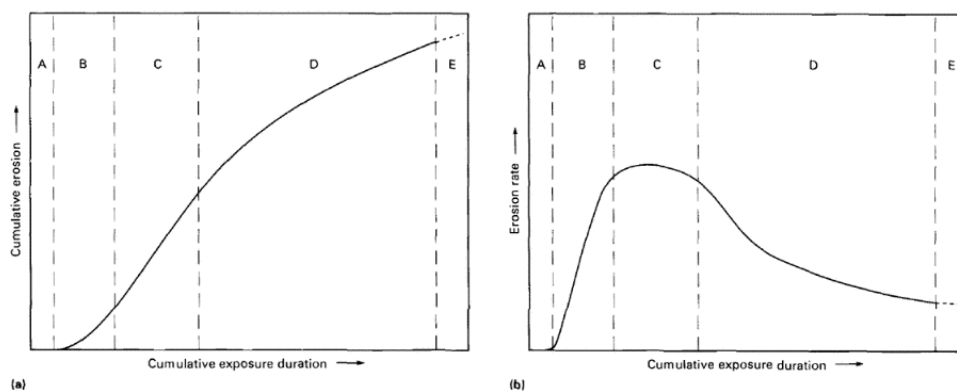


Figure 8. Characteristic erosion versus time curves. (a) Cumulative erosion (mass or volume loss) versus exposure duration. (b) Corresponding instantaneous erosion rate versus exposure duration. The following stages have been identified: (A) incubation stage (B) acceleration stage (C) maximum rate stage (D) deceleration stage; and (E) terminal or final steady-state stage, if assumed to exist. Reprinted from Heymann [36].

It is proven that the maximum pressure on the solid surface due to the impingement of a droplet of diameter 100 μm is damped down by 10% because of the presence of a liquid film with 2.5 μm thickness over the solid material [55]. Furthermore, the erosion in the near field is higher than the erosion rate in the far field, which is due to the higher local flow rate in this area [32].

Impact angle: As explained before the maximum rate of mass loss will happen at an impact angle of 90° [56, 39].

Testing time, nozzle diameter, droplet size and impact velocity are the other important parameters that need to be well-defined when designing a liquid erosion testing machine.

2.6.2. Whirling arm based system

This type of apparatus has been used for the study of liquid droplet impingement erosion by droplets having a diameter larger than 1mm [57]; moving the sample is good way to simulate the impact taking place when a moving object is exposed to a rainfall. The well-known rig which is used for this method is the whirling arm. In the following some of the previous designed systems are explained.

The Whirling Arm Rain Erosion Rig (WARER) was designed and built by University of Limerick [47]. It consists of a rotating arm that carries the sample on the tip of itself (Figure 9). In this machine, water droplets are introduced into the test chamber through 36 blunt dispensing needles with an internal diameter of 0.15 mm [47].

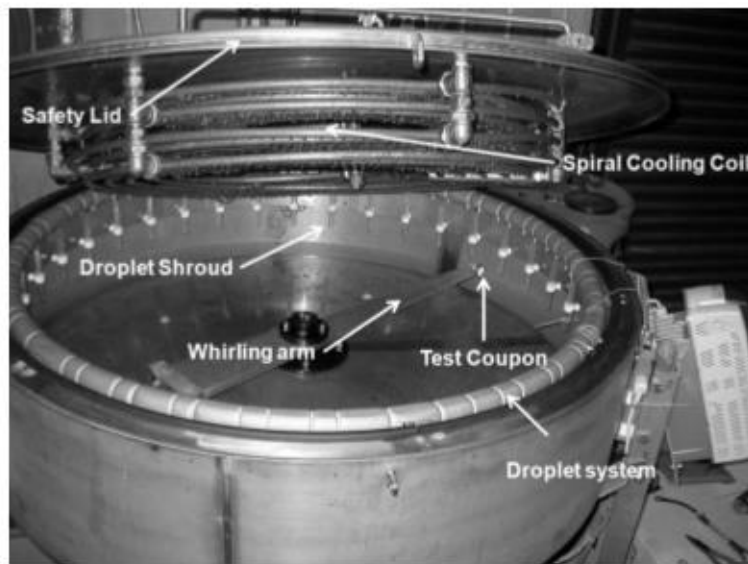


Figure 9. WARER at University of Limerick. Reprinted from Tobin et al. [47] with the permission of Elsevier Publishing.

SAAB is another erosion testing facility (Figure 10); designed in the 1960s it has a prominent history in the field of rain erosion [48]. The sample is placed on a rotating arm at a radius of 2.19 m. The system is able to simulate impact speeds of up to 300 m/s. This system also is able to vary the droplet size and rainfall rate.

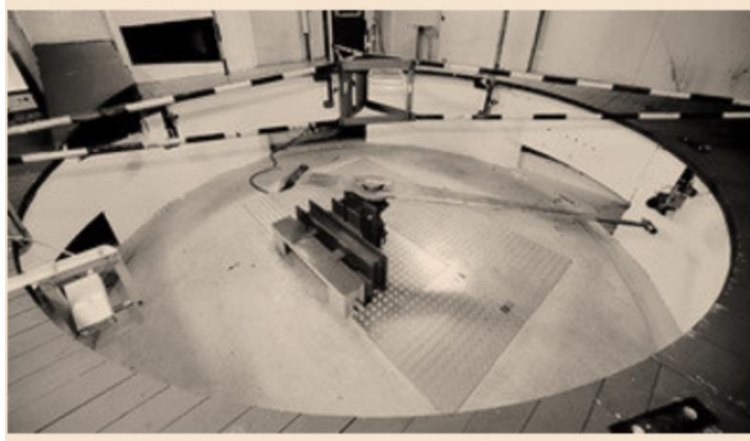


Figure 10. SAAB rain erosion test facility. Reprinted from Tobin et al. [48].

Zhang, et al. [17] designed a laboratory water jet setup to analyse the liquid erosion of blade coatings. In this machine 22 coated panels can be placed on the rotating wheel with the diameter of 52 cm and speed range of 126-160 m/s, Figure 11. In this system, the distance between the nozzle orifice and the sample surface was kept at 10 cm and erosion evaluated by inspecting samples every half an hour. The rainfall intensity is 30-35 mm/h and the water droplet size is 1-2 mm.

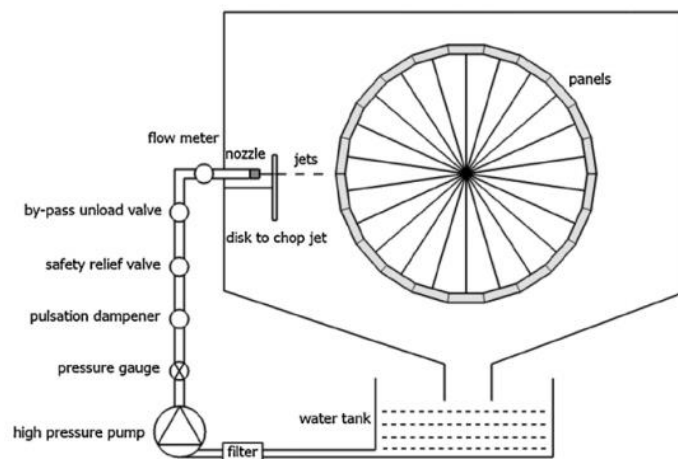


Figure 11. Water jet erosion rig. Reprinted from Zhang et al. [17] with the permission of Elsevier Publishing.

2.6.3. Stationary sample erosion test (SSET)

This apparatus allows the study of the liquid droplet impingement erosion for smaller droplets with diameters in the order of few hundreds of micrometres [32]. This method is simple, economic and reliable (Figure 12). The specimen is fixed and water hits the surface of the specimen through a water jet nozzle.

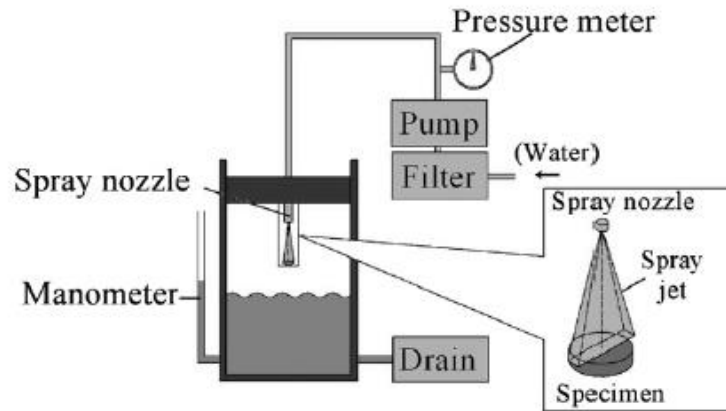


Figure 12. Experimental apparatus for liquid impingement erosion by high speed spray. Reprinted from Fujisawa et al. [32] with the permission of Elsevier Publishing.

Grundwürmer et al. [59] used SSET water jet for liquid erosion testing (see Figure 13). The SSET unit was setup with fixed SOD of 300mm between the nozzle and sample surface, impact angle of 90° and droplet diameters starting from 0.3mm down to below 0.1mm. The water jet was moved across the sample surface at two different feed speeds: 0.017 and 0.25m/s resulting in exposure times of 4.8 and 0.32s per water jet crossing.

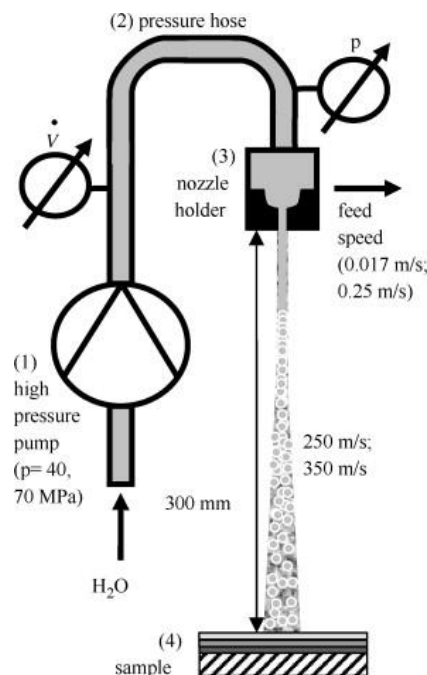


Figure 13. Stationary sample erosion test. Reprinted from Grundwürmer et al. [59] with the permission of Elsevier Publishing.

Fujisawa et al. [33] designed an experimental apparatus for water droplet impingent testing (Figure 14). They setup two different units for their experiments, one unit with a 0.8mm diameter nozzle, SOD of 270mm with the nozzle pressure of 16MPa and the other unit with the same nozzle but SOD of 480mm and nozzle pressure of 28MPa, for both units the impact angle was 90° [33].

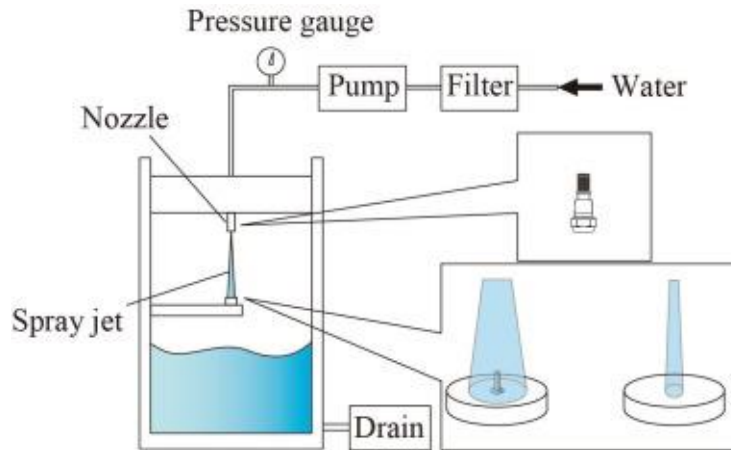


Figure 14. Experimental apparatus for LDI erosion. Reprinted from Fujisawa et al. [33] with the permission of Elsevier publishing. LDI: liquid droplet impingement.

Pulsating Jet Erosion (PJET) is an erosion test facility in which a high pressure water jet is forced through a nozzle of 0.8mm diameter and is subsequently cut into individual water jets by a rotating disc (Figure 15). This system can provide different impact velocity and impact frequency as well [47, 53].

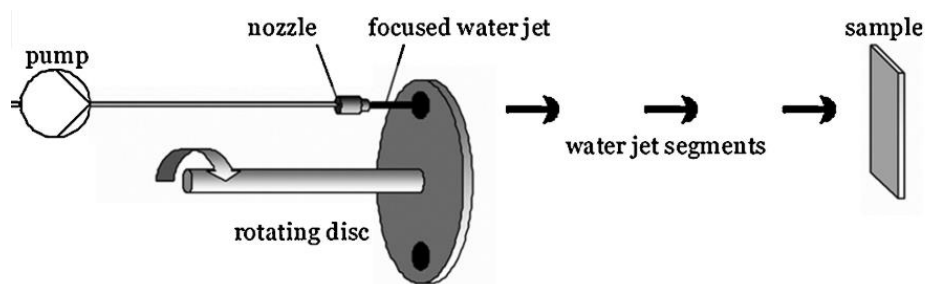


Figure 15. Principle of PJET test method. Reprinted from Tobin et al. [47] with the permission of Elsevier Publishing. PJET: pulsating jet erosion

3. The sol-gel technique

Over the last few decades, the sol-gel techniques have been used for production of a variety of mixed-metal oxides, nanomaterials and nanoscale architectures, nanoporous oxides, and organic-inorganic hybrids. The sol-gel processing is the most convenient manufacturing method because of its simplicity, good mixing of starting materials, relatively low reaction temperature and easy control of chemical composition of the end product. Sol-gel synthesis is utilized to fabricate advanced materials in a wide variety of forms: ultrafine powders, thin film coatings, porous or dense materials.

The sol-gel technique is a wet-chemical technique that can produce polymeric networks of hybrid organic/inorganic materials that can be used as composite coatings. This composite materials which produced by sol-gel techniques have the properties of organic polymers such as flexibility and the properties of inorganic materials such as hardness at the same time. In a sol-gel, solid particles are suspended in a liquid to form a colloidal solution (*sol*) that acts as the precursor to an integrated network (*gel*) of either discrete particles or a

polymer network [58]. The hardness and the flexibility of the sol–gel derived coating can be adjusted by the amount of inorganic-rich compounds as well as by the degree of cross linkage, for example increasing the Non-cross linking organic groups will increase the flexibility of the coating.

The sol–gel process enables the deposition of films and coatings of thicknesses from 0.01-5 μm . The properties of sol–gel derived coatings can be engineered at the molecular level for optimum physical and chemical behaviour, providing control over adhesion, hydrophobicity, permeability, texture, morphology, optical properties and other characteristics [60].

For enhancement of resistance to liquid erosion, the hybrid network provides sufficient mechanical stability to avoid cracks caused by droplet impact and is also flexible enough to absorb the kinetic energy of droplets [59]. Hard ceramic coatings experience higher wear at a 90° impingement angle whilst soft metallic coating experiences higher wear at low impingement angles (e.g., 30°). Therefore, a mixture of a soft polymer matrix containing hard ceramic particles in a composite coating may offer superior protection for different applications. The degree of cross-linking determines the hardness and the mechanical stability of the coatings, which is important to avoid crack initiations in the layer and crack growth [61].

The most promising coatings for commercial applications made using the sol–gel technique are Organically Modified Ceramics (ORMOCER) and Organically Modified Silica (ORMOSIL) [62]:

- (i) Organically Modified Ceramics (ORMOCER) is inorganic-organic composites on a molecular or nano level. The inorganic backbone may be synthesized alkoxides or soluble oxides. Organic components can be introduced through the formation of carbon–silicon bonds, covalent bonds or through electrostatic interactions (i.e. ionic bonding). Introduction of organic polymeric chains leads to a second type of network; this network can be chemically linked to the inorganic backbone or act as an interpenetrating network. Properties of the materials can be varied by changing stoichiometries, reaction conditions and processing. Their applications run from thermoplastic materials (e.g. sealing) to brittle coatings (hard coatings) [63]. The basic properties of ORMOCER[®] which make them very attractive materials for coating applications are their transparency, their good adhesion to various substrates, their chemical stability and their good abrasion resistance due to the inorganic structures in ORMOCER[®] [64].
- (ii) Organically Modified Silica (ORMOSIL), the silica surface consists of two types of functional groups, siloxane (Si-O-Si) and silanol (Si-OH). Thus, silica gel modification can occur via the reaction of a particular molecule with either the siloxane (nucleophilic substitution at the Si) or silanol (direct reaction with the hydroxyl group) functions. Reaction with the silanol group constitutes the most common modification pathway. There are three main methods in which functional groups are attached to the silica surface [2]: (i) reaction of organosilanes or other organic molecules and silica

surface functions, (ii) chlorination of the silica surface followed by reaction of the Si-Cl with an appropriate reactant (e.g. amine or alcohol), (iii) via sol-gel methodology followed by post-modification, wherever necessary [65].

3.1. Advantages of sol- gel technique over traditional techniques

There are several coating methods in the industry, some of them are expensive because of expensive equipment (e.g. plasma spraying), some of them produce low quality coatings (e.g. flame spraying), some methods are not practical to coat the internal surface of the small cylindrical (e.g. high velocity oxygen fuel spraying) and some of them are time consuming and so challenging to produce thin film (e.g. powder coating technique). On the other hand, purely inorganic coating materials are very expensive coatings and they have poor adhesion to substrate due to the difference in thermal expansion coefficient between the coating materials and substrate.

Sol-gel technique is an alternative to traditional coating techniques which makes it possible to produce organic-inorganic hybrid coating [66, 67]. In this method individual coating layers are limited to less than 0.5 μm to prevent cracking and coating failure during thermal processing as a result of trapped organics within the coating [68] which has negligible additional weight on the substrate. Sol-gel derived coating provide excellent adhesive between the metallic layers to the top coat, this is achieved by using precursors containing functional groups which are able to form chemical bonds to the substrate such as epoxy, vinyl and methacrylate. By sol-gel method it is possible to produce coating layer which is thick enough for corrosion protection as well [69]. In this method having the ability to use different silane precursors allows modification of the properties of the gel [70]. Control of stoichiometries allows control of the hardness and the amount of non-cross linking organic groups determines the flexibility of the coating.

In addition, in sol-gel technique mixing is done at the molecular level, so the coating has high purity and uniformity. Sol-gel coatings are normally performed at relatively low temperature, so there is no need to reach the melting point, the method is more energy efficient than other methods of coatings that require temperature approaching melting point of materials [71, 72], temperature can be as low as room temperature up to a maximum of 500 $^{\circ}\text{C}$, which is the upper limit for the temperature stability of the organic groups [73].

This technique (sol-gel) has some disadvantages as well; one of them is the high permeability of the coating and the difficulty in controlling the porosity, which is important as erosion resistance is strongly linked to porosity of the coatings [74]. Shrinkage of the wet gel during curing process can also cause crack formation in the coating structure and finally the sol-gel method is highly substrate-dependent, primarily due to limitations imposed by thermal mismatch between the coating and substrate [69].

3.2. Sol–gel process

Sol–gel process has four steps; a) Preparation of a stable suspension of colloidal particles (sol) in a liquid. b) Depositing the solution on the surface by one of a variety depositing methods and produces the coating. c) Polymerization of the sol through the removal of the stabilizing components and produce a gel in a state of a continuous network. d) Heat treatments to pyrolyze the remaining organic or inorganic components and form an amorphous or crystalline coating.

The reactions in the sol–gel process depend on the parameters such as: nature and concentration of alkoxides, amount of water added, type of the catalyst used, sequence of adding components, mixing schedule and temperature.

3.3. Techniques for deposition of sol–gel coatings

3.3.1. Dip coating technique is a process where the substrate, which needs to be coated, is immersed in a liquid and then withdrawn with a well-defined withdrawal speed. This process is performed under controlled temperature and atmospheric conditions (Figure 16). In this technique, two parameters control the thickness of the coating: the viscosity of the liquid and the angle between the substrate and liquid surface. This method is suitable for coating the curved surfaces like bulbs, eyeglass lenses and bottles.

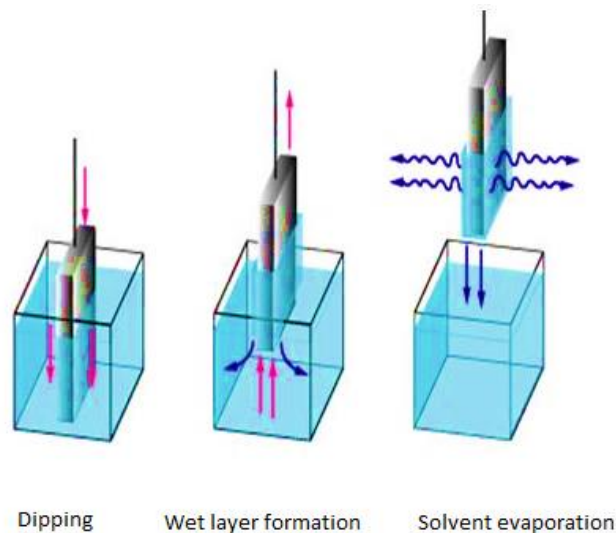


Figure 16. Dip coating process. Reprinted from Attia et al. [72].

When the viscosity and speed is high, the coating thickness can be estimated by:

$$h = c_1 \left(\frac{\eta U_o}{\rho g} \right)^{1/2} \quad (6)$$

Where $c_1 = 0.8$ for Newtonian fluids.

When the substrate speed and viscosity is low, as is the case for sol–gel process, the coating thickness can be found from:

$$h = 0.94 \frac{(\eta U_o)^{2/3}}{\gamma_{LV}^{1/6} (\rho g)^{1/2}} \quad (7)$$

In the above h = the coating thickness, η = viscosity of the sol-gel, U_o = substrate speed, and γ_{LV} = liquid-vapour surface tension.

3.3.2. Spin coating technique

Spin coating is an incredibly effective technique for producing high quality, uniform thin films. In this technique, the substrate spins around an axis, which should be perpendicular to the coating area (Figure 17).

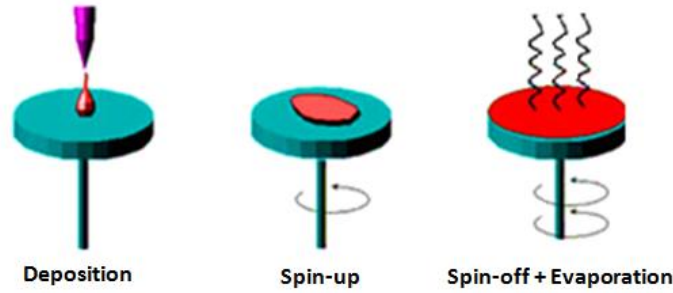


Figure 17. Spin coating process. Reprinted from Attia et al. [72].

This technique has four steps: deposition of the sol, spin up, spin off and gelation by solvent evaporation. In comparison with the dip-coating method, spin coating technique can produce homogeneous thin coatings, even for non-planar substrates. A model is presented for the description of thin films prepared from solution by spinning; using only the centrifugal force, linear shear forces, and uniform evaporation of the solvent, Meyerhofer [75] split the spin coating into two stages: one controlled predominantly by viscous flow and the second controlled by evaporation. He calculated the final thickness of the film as functions of the various processing parameters as:

$$h = \left(1 - \frac{\rho_A}{\rho_{A_0}}\right) \times \left(\frac{3\eta \cdot m}{2\rho_{A_0} \cdot \omega^2}\right)^{1/3} \quad (8)$$

Where h is final thickness, ρ_A is the mass of volatile solvent per unit volume, and ρ_{A_0} is its initial value, ω is the angular velocity, m is the evaporation rate of the solvent found empirically.

Bornside, Macosko, and Scriven [76] predicted film thickness based on the initial properties of the polymer solution, solvent, and spin speed. They reported a wet film thickness, h_w , at which the film is supposed to become immobile can be found from:

$$h_w = \left[\left(\frac{3\eta_0}{2\rho\omega^2}\right) \kappa(x_1^0 - x_{1\infty})\right]^{1/3} \quad (9)$$

where κ is the mass transfer coefficient, x_1^0 is the initial solvent mass fraction in the coating solution, $x_{1\infty}$ is the solvent mass fraction that would be in equilibrium with the solvent mass

fraction in the gas phase. Further film thinning is only due to evaporation; therefore, the final film thickness, h_f , is

$$h_f = (1 - x_1^0) h_w \quad (10)$$

The above analytical model proposed was found to agree within 10% over the whole film thickness range [77].

3.3.3. Flow coating process

In this method the coating liquid is poured over the substrate. The thickness of the coating depends on the angle of inclination of the substrate, the coating liquid viscosity and the solvent evaporation rate. In this technique usually after the coating, spinning the substrate helps to generate a more homogeneous coating, otherwise the thickness of the coating will increase from the top of the substrate to the bottom (Figure 18).

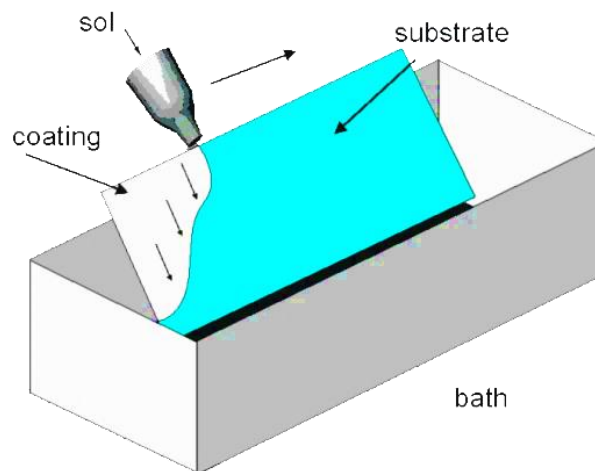


Figure 18. Sol- Gel, flow coating technique. Reprinted from Attia et al. [72].

3.3.4. Spray coating technique

This method is used widely in the industry and is suitable for coating irregularly shaped objects. In comparison with the dip-coating method, this method is faster and wastes less of the sol material.

3.3.5. Capillary coating technique:

In previous four methods there is some wastage of the coating liquid, e.g. in the spray coating, 100% overspray is done [72], while in dip coating and flow coating only 10% to 20% of the coating liquid is used in the fabrication of the final coating. This waste can be overcome using the capillary technique, **Figure 19**. In this method, the substrate is held upside down by the help of a chuck and then a tubular dispersal unit is moved gently under the surface of the substrate and deposits the coating liquid on to the surface. A solution reservoir collects the excess of fluid and pumps it back into the system to ensure that the deposition of the solution is continuous during the process [72].

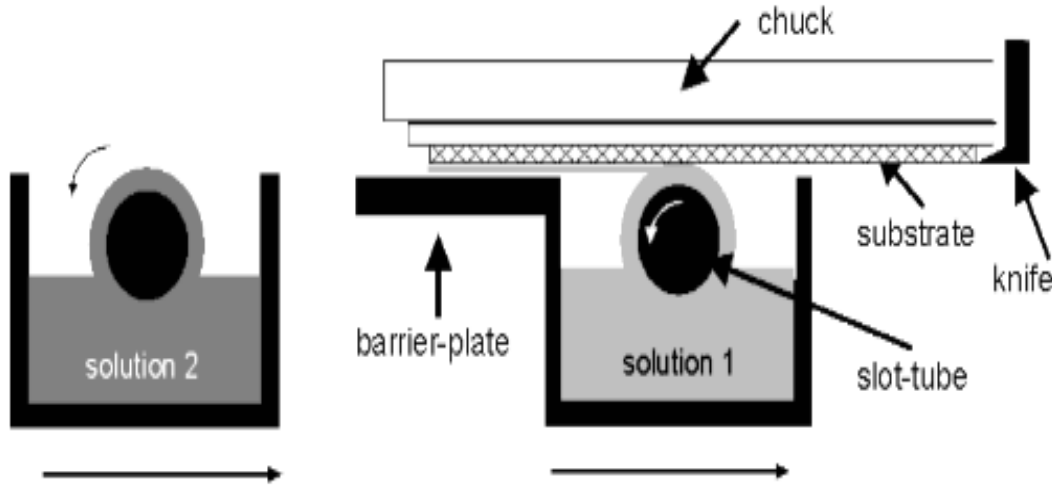


Figure 19. Sol-gel capillary coating technique. Reprinted from Attia et al. [72].

The coating thickness depends on the deposition rate v_d according to equation:

$$h = \kappa \times v_d^a \quad (11)$$

where the exponent a and empirical factor k are dependent on the viscosity, surface tension and density of the fluid used.

3.3.6. Roll coating technique

In this technique, the liquid flows into a narrow gap between two rotating cylinders. This method is good for the painting, photographic and tape-recording industry, where coating of a large surface area with one or several uniform layers is desired.

The coating quality strongly depends on the substrate preparation; for that reason using solvent cleaning or sand blasting and surface activation through plasma treatment are strongly suggested before coating to remove the dust and organic materials such as oil stains from the substrate and also improve the adhesion properties through the addition of functional groups to the substrate.

3.4. Sol-gel applications

Sol-gel coatings are considered as potential candidates to substitute environmentally unfriendly chromate surface treatments for metallic substrates. These coatings are used for different purposes as explained below.

Wear resistant coating: This technique is used to manufacture erosion, corrosion and abrasion resistant coatings to protect substrates such as wind turbine blades, aeronautic structures, submarine body, low-carbon structures and mild steel industrial components [58, 59, 71].

Hydrophobic coating: Coatings with water repellent properties are being increasingly used to serve as protective coatings on windows, car windshields, solar panels, building exteriors, wind turbine blades and other large outdoor surfaces. Sol-gel technology is the preferred route to produce such coatings; for instance Dou et al. [78] developed a single-layer hydrophobic antireflective SiO₂ coating prepared by sol-gel method with 300nm thickness,

97% transmittance and large static water contact angle of 130.6° to improve the optical performance of the optical system efficiency by restrain the absorption of the moisture in the air.

Anti-fog coating: The sol–gel process are also used to produce hydrophilic coatings on glass materials by dispersing the water across the surface and preventing aggregated water molecules to be seen as a droplet and produce fog. There are variety of applications for these glasses e.g. optical lenses, eyeglasses, bathroom mirrors, covers for headlights and vehicle windows.

Self-cleaning coating: This coating has many applications in different industries like textiles, paints, window glasses and cements. This coating saves the costs of cleaning and also increases the duration of woven products. The self-cleaning coating can be hydrophobic or hydrophilic.

Antimicrobial coating: This coating is important to reduce the presence of bacteria on different surfaces that people touch in their daily life, For example, using silver-titanium dioxide nano-coating in subway train interiors reduces the presence of bacteria by up to 60% [79].

Anti-stain coating: This coating has wide applications in different industries such as textile, construction, automotive and electronic because of stain-resistant and hydrophobic characteristics. Anti-stain coatings are hydrophobic coating and they are able to decrease the attachment of the foreign particles to the surface. In this area using organic- inorganic hybrid systems are attractive because they can improve the quality of the coating. For example polyimide/silica hybrid anti- stain coating which synthesized by sol–gel method has characteristics such as hydrophobic, hydrophilicity and optical transparency [79].

Self-healing coating: One of the most important problems with the polymer composites in structural applications is the formation of micro cracks. From engineering point of view, the ability to repair micro cracks can increase the lifetime, safety and durability of a structure. Self-healing materials are able to repair and recover structural ability after damage. Self-healing can be done in a form of capsule or vascular which are different in term of the damage volume that can be healed, repeatability of the healing process and the recovery rate for each approach [79].

3.5. Evaluation of mechanical properties of sol–gel derived coatings

The mechanical properties of the sol–gel derived coatings strongly depend on the residual stress in the coating [80]. It has been reported that stress is induced in the coating on deposition and it increases as the coatings are consolidated during the curing process and even during the heat treatment condition [81]. The total stress in the coating is the sum of stress developed after the evaporation of the solvents during drying. The stress causes shrinkage of the coating [82]. The stress within the coating also depends on the density of the coating material, heat treatment temperature (increasing the heat treatment temperature will increase the stress level in the coating), water-precursor ratio (higher water precursor ratio will result in a higher level of stress in the coating), coating thickness

(increasing the thickness of the coating will increase the level of stress in the coating). The stress should be kept as low as possible in order to produce a good coating [80].

For the mechanical properties evaluation of the sol–gel derived coatings the following tests are commonly performed:

- The adhesion properties of the coating,
- Pencil hardness test
- Abrasion resistance

3.5.1. Evaluation of adhesion of sol–gel coatings to substrate

The adhesive bonding of the coating to the substrate is assessed by the amount of force required to separate the coating from substrate. Coating can fail in two ways: interface debonding of the coating from the substrate and cohesive failure due to crack propagation through the coating [67]. This can be analysed using different tests as described below.

Indentation test: This test is used to analyse the adhesion in relation to the performance of real engineering components in service [83]. Fracture toughness can be measured from the interfacial cracking when the film cracks during indentation.

Scratch test: This test is used to analyse the adhesive properties of the coating (Figure 20), the results are influenced by : coating thickness, substrate mechanical properties, interfacial bond strength and test conditions such as scratch speed, load and indenter tip radius [67].

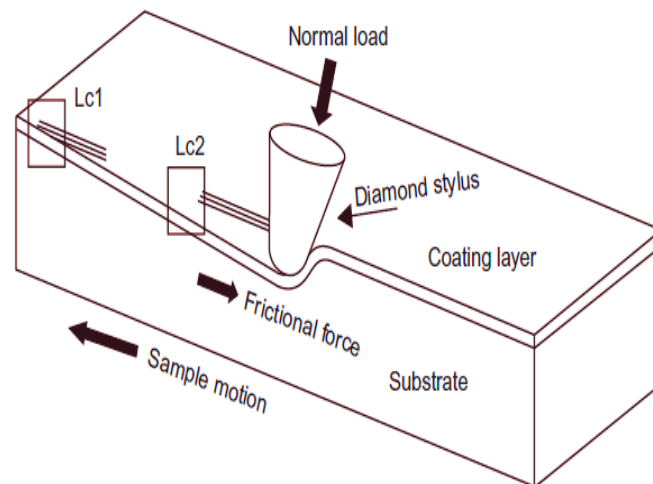


Figure 20. Schematic diagram showing the indenter scratching the work piece. Reprinted from Kalidindi et al. [67] with the permission of Elsevier Publishing.

Cross-hatch cut and scotch tape test: This is a standard test for the evaluation of the adhesive properties of a coating involving the measurement of the material removed from the square grid by using a cutter with sharp cutting edges spaced at 1mm from each other that pressed against the coating and scratched to make deep groove. This test is based on the material removal and adhesion of the coating, which is ranked from 5B (excellent adhesion) to the 0B (very poor adhesion) as shown in Table 1.

Table 1. Classification of adhesion level of the coating by cross-hatch cutting [84].

5B	Excellent adhesion
4B	<5% material removed
3B	5-15% material removed
2B	15-35% material removed
1B	35-65% material removed
0B	>65% material removed

UV: ultraviolet; MW: microwave.

Pull-off adhesion test: This test is used to if a coating is fit for service. The result is often critical to the acceptance or rejection of a coating process, as the adhesion value quoted by the coating manufacturer can be adversely affected by aspects of the coating process. Low adhesion values are indicative of inadequate surface preparation of the substrate.

In this test a test dolly is glued to the coated surface and then a perpendicular tensile force is applied to the surface in an effort to remove both the dolly and the coating from the substrate. ASTM D4541 and BS EN ISO 4624 describe several different test apparatus. A measure of the adhesion of the coating system is the force at which the coating fails and the type of failure obtained.

3.5.2. Evaluation of hardness of sol–gel coatings by pencil hardness test

This test measures the hardness of the sol–gel and other organic coating on any rigid substrate. According to the standard ASTM D3363-05 (200) for this measurement a set of pencils with increasing order of hardness are used (9B to 9H) to make a scratch on the coated substrate by holding the pencil firmly in a rolling holder at 45° to the ground and pushed for a scratch length of 6.5mm.

3.5.3. Evaluation of abrasion resistance of sol–gel coatings

Crockmeter and Taber tests are the most common tests for analysing the abrasion resistance of sol–gel nanocomposite coatings.

Crockmeter test: This test employs a 10mm diameter finger rubbing on a flat work piece in a reciprocating motion. In this method, a normal load of 4.5N for a minimum stroke length of 20mm is applied to the work piece.

Taber test: The advantage of this test over the Crockmeter test is quantification of the worn surface by measuring the weight of the sample before and after the test. In this test, two loading arms are provided for applying normal load and holding abrasive wheels of 52mm diameter and a width of 12.7mm on the specimens. There are different grades of abrasive wheels for this test, which are: CS17 for hard coatings and CS10, CS10F for relatively soft coatings [85].

3.6. Sol-gel fast curing

Typically, sol-gel coated surfaces need a separate curing treatment involving heating at temperatures between 100 to 200°C. This treatment increases the manufacturing costs, especially when a sol-gel coating is applied to already existing production chains, but it can make a major contribution to the enhancement of the sol-gel coatings properties such as their hardness and adhesion [86]. For instance for the silane base coating, formation of the -Si-O-Si- siloxane chains through the condensation of excess silanol groups can result in a dense network layer that can be act as a barrier against species like water drops. This dense layer can be formed upon curing, so the curing time and temperature are key factors of this process. If the curing period was inadequate, the result would be a porous film with low cross-linking density. On the other hand, if the curing time and temperature exceed the optimum range, it might lead to formation of a brittle film. A variety of curing techniques have been used including thermal curing, ultraviolet (UV) curing, microwave (MW) curing, dual process (UV+ microwave) and infrared curing [66]. A fast curing technique is a major commercial requirement; the short curing times for UV and microwave techniques means they are preferred to thermal methods even though they provide coating with the lower pencil scratch hardness [66].

UV curing: This is a clean and fast technique, which provides a high quality finishing [87]. UV curing has some advantages over the traditional methods, such as: high speed, easy to control, energy efficient, low temperature needed, no solvent needed (as curing process done by polymerization) and the high finishing quality. Factors that affect the curing rate are: monomer component in the UV resin, coating thickness and the intensity of UV per unit area. It should be mention that the UV energy decreases exponentially with depth and the curing speed will increase with the amount of UV energy per unit area at a non-linear rate.

Cakir [88] used a UV curing technique to cure the sol-gel derived hybrid polymer based coating, which used to cover the aluminium substrate. He first heated the coating at 35°C in a vacuum oven for about 10 minutes to remove the trapped air from the mixing process and then UV curing process was performed by using a medium pressure mercury lamp (150 w/cm, λ_{\max} : 320-390 nm), with the speed conveyor belt of 5m/min.

Microwave curing: Microwaves are electromagnetic waves with a frequency from 300 MHz to 300 GHz. Sowntharya, et al. [66] performed four different curing processes to analyse the effect of each one on the coating (Table 2). As can be seen in the Table 3, when MW or UV curing methods were used alone, samples showed very poor pencil scratch hardness, even lower than the substrate scratch hardness, but by using a dual curing process, it was increased. Samples, which are thermally cured, show greater hardness in comparison with the samples that are cured by dual curing methods because of the curing time, dual curing technique is preferable to the thermal curing method as it is a fast curing technique.

Table 2. Setup of four different curing techniques [66].

Method of curing	Process setup
Thermal treatment	Temperature of 130°C curing time: 4 hours
UV curing	Three- medium- pressure- mercury lamp (120w/cm), belt speed: 2m/min curing time: 4 minutes
Microwave curing	Using domestic Panasonic microwave oven curing time: 2 minutes
MW+UV curing	Microwave curing on one side followed by UV curing on both sides

UV: ultraviolet; MW: microwave.

Table 3. Thickness and pencil hardness of SiO₂-TiO₂ hybrid coatings cured by different methods [66].

Curing method	Withdrawal speed (mm/s)	Average thickness (μm)	Pencil scratch hardness
Thermal curing	1	2.3 \pm 0.2	H
	3	4.6 \pm 0.1	2H
	6	7.2 \pm 0.07	3H
MW (or) UV	1	-NA-	<2B
	3		
	6		
MW+UV	1	2 \pm 0.1	H
	3	3.4 \pm 0.3	H
	6	5.8 \pm 0.3	2H

UV: ultraviolet; MW: microwave.

4. Sol-gel with additive carbon nanotubes and graphene nanoparticles

In sol-gel coatings, the hardness and mechanical resistance can be increased by adding nanoparticle reinforcement to the coating [59]. Many researchers have developed different methods of dissolving the additive nanoparticles in an appropriate solvent and then made hybrid materials, which take advantage of the exceptional material properties of the nanoparticles. As a result, they improved the mechanical, thermal and electrical properties of the coating.

In this section, the review is focused on previous works on using carbon nanoparticles (CNPs), specifically carbon nanotubes (CNTs) and graphene for improving the erosion resistance of coatings.

4.1. Carbon nanoparticles (CNPs)

In the last two decades, many researchers have investigated nanomaterials, with diameters less than 100 nm, as additives in the manufacturing of coatings [89]. There is a variety of nano-materials interesting properties. Among them, one of the most promising is carbon nanoparticles (CNPs) [90]. With their attractive properties such as nanoscale diameter, high aspect ratio, low-weight, high electrical conductivity, and extraordinary mechanical, optical, and thermal properties, carbon nanotubes (CNTs) and graphene have attracted much attention in the last decade. Many investigations have shown that a small amount of these nanomaterials resulted in a dramatic improvement in the electro-mechanical properties of their composite materials. However, due to their agglomeration or tangled coils as a result of strong van der Waals interactions, their functionalisation is essential in achieving proper dispersion in polymer matrices and obtaining outstanding electro-mechanical properties.

Figure 21 displays the number of published research papers recorded on Scopus containing the word carbon nanotubes, CNT and graphene from 2010 to 2017. It is clear that in recent years, more attention is devoted to graphene and the ratio of Graphene/CNT published works in 2017 is 2.27 while the number of CNT published work is stabilized around 5300 articles.

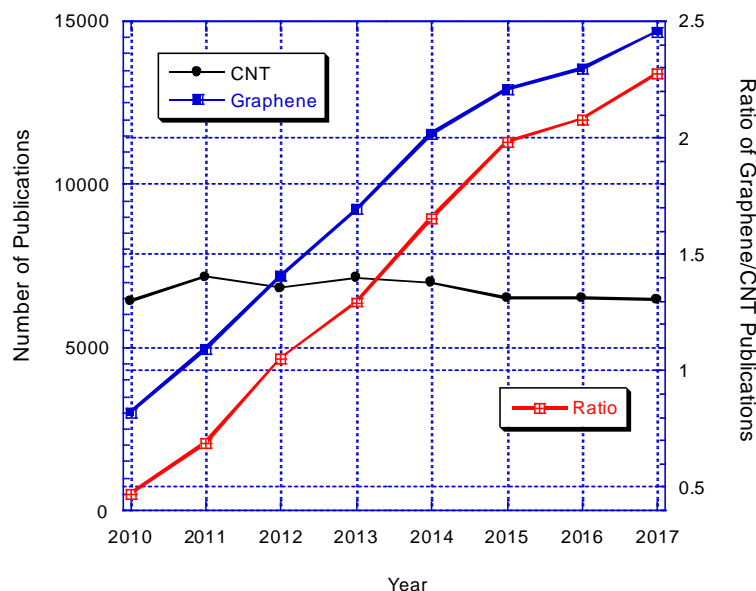


Figure 21. Number of publications with titles including “carbon nanotubes” and “graphene”.

4.1.1 Carbon nanotubes (CNTs)

CNT are an allotrope of carbon and have a long one-dimensional cylindrical tube shape of carbon atoms [91]. Carbon nanotubes are classified as single-walled (SWCNTs) originally reported in 1993 [92], and multi-walled (MWCNTs) first discovered in 1991 both by Iijima

[93]. SWCNTs are created by rolling a single layer of graphite into a seamless cylinder. SWCNTs have two separate regions, side-wall of the tube and its end cap. The transmission electron microscope (TEM) images of a SWCNT and a MWCNT are shown in Figure 22 [94].

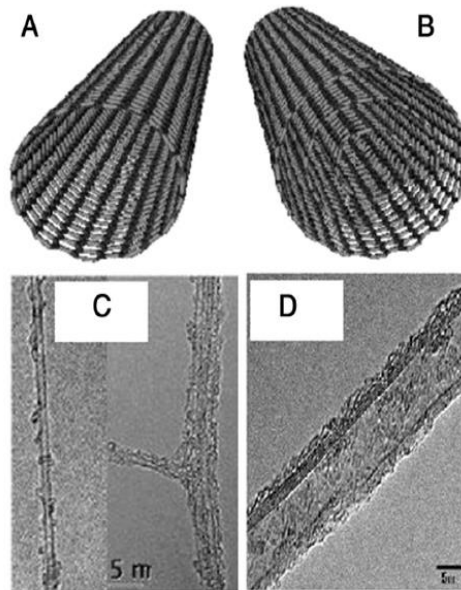


Figure 22. Schematic structure of (a) SWCNT and (b) MWCNT. The TEM images of (c) SWCNT and (d) MWCNT. Reprinted from Eatemadi et al. [94] with the permission of Springer Publishing. TEM: transmission electron microscopy; SWCNT: single-walled carbon nanotube; MWCNT: multi-walled carbon nanotube.

In the SWCNT structure, covalent bonds are acting like a beam element between the carbon atoms, resisting stretching, bending and torsion [81]. The morphology of SWCNT is classified according to the way that the single layer of graphite sheet (hexagonal structures) is wrapped into a cylindrical tube and capped with half shape of fullerene structure [95]. The orientation and magnitude of chiral vector $C = na_1 + ma_2$ in graphene sheet defines the morphology of carbon nanotubes where (n, m) are integers and for $(n, 0)$ makes zig-zag, for (n, n) makes armchair and for (n, m) makes chiral [96]. The diameter of a carbon tube can be calculated from

$$d = \frac{a}{\pi} \sqrt{m^2 + mn + n^2} = 0.783 \sqrt{m^2 + mn + n^2} \quad (12)$$

where $a = 1.42\sqrt{3} \text{ \AA}$ corresponds to the lattice constant in the graphite sheet (the C-C sp^2 bond length is 1.42 \AA). m and n are a pair of indices that describe the chiral vector.

On the other hand, MWCNTs consist of multiple layers of graphene that form concentric tubes. Depending on the number of layers, the inner diameter varies from 0.4 nm up to a few nanometres and the outer diameter varies from 2 nm up to 30nm. Also the distance between the graphene layers is approximately 0.34 nm to 0.39 nm [94]. MWCNTs can be found in two structural models; Russian doll model which is when a carbon nanotube contains another nanotube inside it with a smaller diameter than the outer one and Parchment model is the one when a single graphene sheet is wrapped around itself manifold like a rolled up scroll of paper [94].

CNTs have high tensile strength and are as strong as a carbon-carbon bond. In Table 4 the material properties of SWCNTs and MWCNTs are compared with graphene and stainless steel [97].

CNTs are used in many different areas including the fabrication of flat panel displays, gas storage devices, toxic gas sensors, lithium batteries, advanced polymer matrices, lightweight composites, conducting paints and electronic nanodevices, etc.

Table 4. Comparison of CNTs and graphene material properties with stainless steel.

Material property	SWCNT	MWCNT	Graphene	Stainless Steel
Young's modulus (TPa)	1-5	0.2-0.9	125	0.186-0.264
Tensile strength (GPa)	13-53	63-150	150	0.38-1.55
Thermal conductivity (W/m K @RT)	3500	3180	5000	16-24
Electrical conductivity (S/m @RT)	10 ⁷		10 ⁸	1.45×10 ⁶
Thermal stability	up to 2800 °C in vacuum		500 °C	

CNT: carbon nanotube; SWCNT: single-walled carbon nanotube; MWCNT: multi-walled carbon nanotube.

4.1.2 Graphene

Graphene is a two dimensional allotrope of carbon which is only one carbon atom thick and arranged in a hexagonal lattice [91], first discovered in 2004 [98]. Graphene is super strong, about 200 times stronger than steel, and has a very high stiffness. It is believed that graphene and CNTs are two of the toughest materials ever tested to date [99]. Graphene is highly transparent, extremely light and an excellent conductor of heat and electricity. Graphene has the highest thermal conductivity of all carbon allotropes and it can carry heat better than any other material [98]. It is possible to stretch the graphene by 25% of its original length without any breakage happening in its structure. Because of the superior mechanical properties of the graphene, it is used to produce hybrid composites which are stronger, tougher, thinner and also lighter than the existing composites. Graphene is also used to increase the electrical conductivity of the composites as well [99].

4.1.3 Functionalization of CNTs and graphene

When introducing the individual CNPs into a polymer matrix, it is important to achieve thorough dispersion of the CNPs and strong interfacial interactions between the CNPs and the host polymer matrices. However, due to strong van der Waals forces, it is difficult to disperse CNTs and graphene into the matrix. Therefore, surface functionalisation of CNPs is required in the fabrication of nanocomposite coatings.

Usually after purification of CNTs, to increase the solubility of the CNTs further chemical treatments are needed. These chemical treatments are called surface modification of CNTs which increases the solubility of the CNTs in most organic and aqueous solvent [100]. Different methods for functionalising CNPs have been developed Figure 23. These methods include chemical, mechanical, electrochemical, and irritation reactions. Using these methods, the carbon surface can be activated for subsequent interaction with the host matrix through covalent bonding or non-covalent interactions [101]. Covalent functionalisation is done by directly binding heteroatoms or functional moieties to the carbon lattices by chemical modification. Amino-functionalisation of CNTs enhances the activity of the CNT as both modifier and cross linker to form covalent bonding with host polymer matrix.

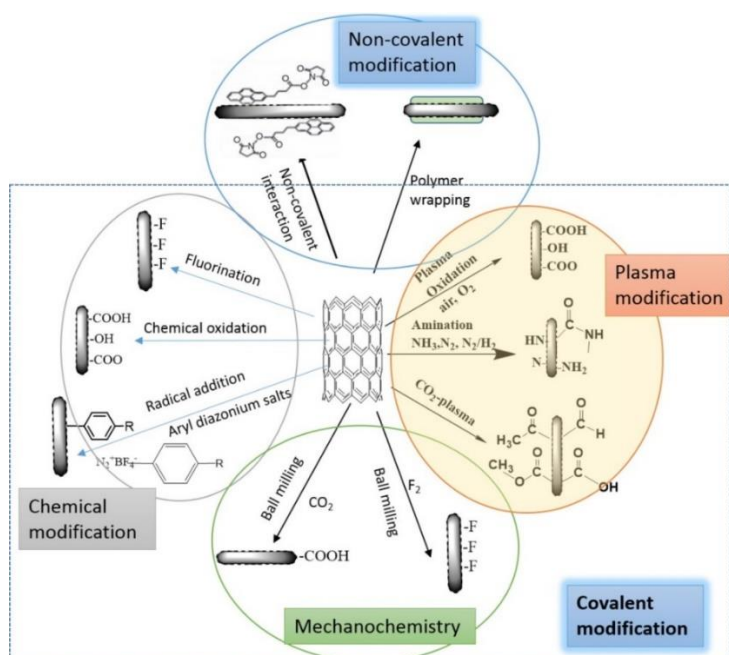


Figure 23. Different surface functionalisation methods for CNPs. Reprinted from Alam et al. [101] with the permission of Elsevier Publishing. CNT: carbon nanotube.

The functionalisation efficiency can be characterised and quantified using a range of analytical techniques, including: X-ray photoelectron spectroscopy (XPS), thermogravimetric analysis (TGA), Raman spectroscopy, Fourier transform infrared spectroscopy (FTIR), transmission electron microscopy (TEM), scanning electron microscopy (SEM), atomic force microscopy (AFM), X-ray diffraction (XRD), contact angle measurement and Brunauer-Emmett-Teller (BET) surface area measurements. TGA is commonly used for quantitative determination of grafting molecules bound to the surface of nanomaterials [102]. High residual char content is representative of a high amount of carbon skeleton while the mass losses can be related to the mass of grafted molecules. The extent of functionalisation can be determined using the following equation [103]:

$$R = \frac{x/M_a}{1-x/M_c} \times 100\% \quad (13)$$

where R is the graft ratio, x is the weight loss of the CNP, M_a and M_c are the atomic weight of carbon and molecular weight of the grafting molecule, respectively.

In chemical oxidation functionalization, the distribution and the nature of the functional groups on the surface of CNTs are highly dependent on the type of oxidant used. As can be seen in the Figure 24, different oxidants affect the distribution of functional groups on the surface of MWCNTs [104]. MWCNTs oxidised with $(\text{NH}_4)_2\text{S}_2\text{O}_8$, H_2O_2 and O_3 yielded higher concentrations of carbonyl and hydroxyl functional groups while HNO_3 , $\text{H}_2\text{SO}_4/\text{HNO}_3$ and KMnO_4 formed higher fractional concentration of carboxyl groups [104]. However, such modification is detrimental to the intrinsic optical, electrical and thermal conductivity properties of CNTs.

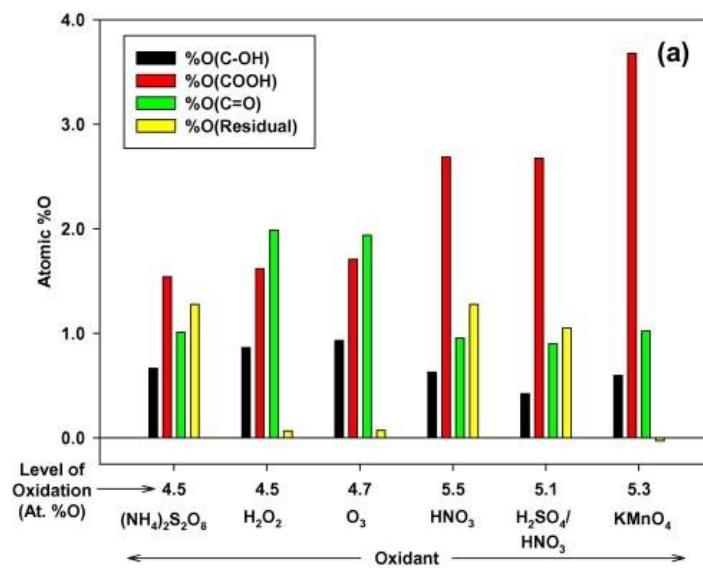


Figure 24. Influence of the oxidant on the distribution of oxygen-containing functional groups on the surface of MWCNTs. Reprinted from Wepasnick et al. [104] with the permission of Elsevier Publishing. MWCNT: multi-walled carbon nanotube.

In the Table 5 some of these chemical oxidation techniques and their procedure are summarised.

Table 5. Summary of different oxidation procedures to functionalize MWCNTs.

Source	Oxidant	Procedure
Rosca et al. [100]	HNO_3	0.2g MWCNTs were dispersed for 30min in 100ml HNO_3 and heated under reflux. Then the sample was filtered in a membrane filter and washed to neutral pH and dried at 120°C for 12h.
Smith et al. [105]	HNO_3	100mg of MWCNTs were sonicated in 200ml of 70% HNO_3 for 1h and then the mixture was heated under reflux for 1.5h at 140°C .

Domun et al. [106]	HNO ₃	0.1g of MWCNTs were dispersed in 100ml of HNO ₃ (70%) and heated under reflux at 135°C for 24h. Then the mixture was filtered and dried in vacuum at 40°C.
Hiura et al. [107]	KMnO ₄	100mg of MWCNTs were sonicated in 200ml of 0.5M KMnO ₄ for 30min. The MWCNT/ KMnO ₄ mixture was then heated under reflux for 5h at 150°C. After cooling down the reaction to the room temperature, 10ml of concentrated HCl was added to dissolve the MnO ₂ by product.
Blanchard et al. [108]	H ₂ SO ₄ /HNO ₃ (3:1)	H ₂ SO ₄ and HNO ₃ were combined in 3:1 ratio to create the solution with a final volume of 8ml. 100mg MWCNTs were added to this solution and the mixture was heated to 70°C for 8h without stirring.
Arabi [109]	H ₂ SO ₄ /HNO ₃ (4:1)	5g of MWCNT were dispersed in 400ml sulfuric acid and 100ml nitric acid in a glass vial and placed in an ultrasonic bath for 3h. Ice was then added to the mixture stored for 24h at ambient temperature. Afterward the mixture was neutralised and dried at 60°C.
Kathi et al. [72]	H ₂ SO ₄ /HNO ₃ (3:2)	3g of MWCNTs were dispersed in 300mL of concentrated H ₂ SO ₄ /HNO ₃ solution at 50 °C and stirred for 20h. The solution was filtered and remaining solid particles washed with water and acetone. Then f-MWCNTs were dried under vacuum at 100 °C for 24h. After that about 0.050 g of f-MWCNTs was dispersed in 50mL of ethanol via ultrasonication for 30min.
Peng et al. [110]	H ₂ O ₂	100mg MWCNTs were added to 15ml of 30% H ₂ O ₂ and the mixture heated to 70°C for 4 days with continuous stirring. Every 24h, 1-5 ml of 30% H ₂ O ₂ was added to the solution for the volume lost due to the evaporation.
Kirk JZ et al. [111]	(NH ₄) ₂ S ₂ O ₈	50mg MWCNTs were added to 50ml of piranha solution (4:1 96% H ₂ SO ₄ : 30% H ₂ O ₂) and stirred for 4h at 80°C.

SWCNT: single-walled carbon nanotube; MWCNT: multi-walled carbon nanotube.

Amine-functionalised CNTs may be covalently bonded to polymer matrices, such as polyepoxides, polyimides, and polyamide [112]. Amine-functionalised graphene CNTs have been used as reinforcing agents, cross linkers and in catalysis, and play multiple functions in epoxy composites [113].

Functional groups can be created on the carbon surface as a consequence of mechanical grinding and shearing. Ball-milling exfoliates graphite into multi-layer carbon nanoplatelets [114] and breaks MWCNT agglomerates under certain treatment conditions (e.g. duration, temperature, and organic modifiers), generating functional groups on the carbon surface. Similar levels of dispersion of MWCNTs were found for those treated by ball-milling for 20 min with those treated with concentrated acids for 120min, but the MWCNTs were highly shortened after ball-milling [115].

The edges of graphene nanoplatelets (GNPs) can be functionalised by ball-milling of graphite in the presence of hydrogen, carbon dioxide, sulfur trioxide and/or carbon dioxide/sulfur trioxide. The amount of functional groups formed was around 65–87 wt%, determined from TGA at 800°C in nitrogen. From Raman spectroscopy, the intensity ratios I_D/I_G of the D-band (1350 cm^{-1}) to G-band (1584 cm^{-1}) were in the range 0.79–1.50 [116], indicating a significant size reduction in platelet size due to mechanochemical cracking and edge distortion.

In addition to the wet-chemistry and mechanochemistry methods, cold plasma, especially low-pressure plasma treatments have become one of the key technologies for surface modification of materials. The highly energised gas species of the plasma can penetrate and break covalent bonds to a depth of several nanometres. The activated surface can then readily react with the excited gas species to form functional groups. The level of surface functionalisation is determined by the gas type and treatment parameters such as pressure, power input, flow rate and time [117].

Different plasmas can introduce different functional groups onto the surface, as shown in Figure 25 [101]. For surface modification, a variety of inert gases such as oxygen-containing gases including O_2 , CO_2 and H_2O ; nitrogen-containing gases including NH_3 and N_2 , as well as other gases such as H_2 , Ar, P and He have been investigated. Fluoro- or hydrocarbon containing gases such as BF_3 , CF_4 , styrene, allylamine, acrylic acid or maleic anhydride can induce plasma polymerisation reactions to form pinhole free polymer nanocoatings on the surface. Ammonia, sometimes in a mixture with other gases (N_2 , Ar, O_2 , CF_4), is often used as precursor to introduce amine functionality to CNPs to enhance hydrophilicity and biocompatibility [117]. Oxygen plasma treatment can generate oxygen-containing functional groups such as $-\text{COOH}$, $\text{C}=\text{O}$, $-\text{OH}$, $\text{C}-\text{O}-\text{C}$, and $-\text{CO}_3$ on the surface of carbon, providing a reaction platform for further interaction with polymers. Ammonia, N_2 , and N_2/H_2 plasmas introduce primary, secondary and tertiary amines, as well as amides [118].

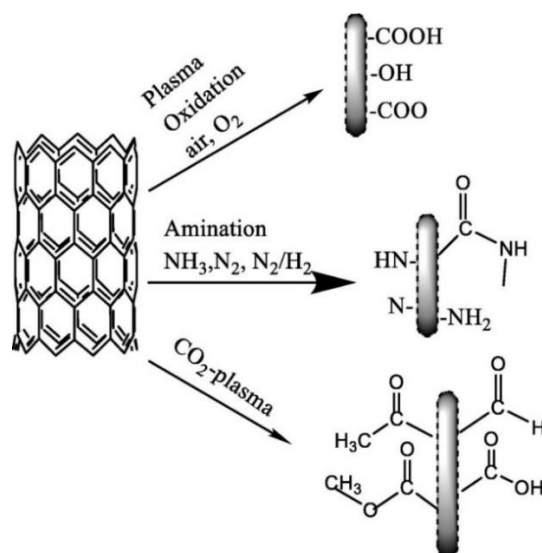


Figure 25. Possible functional groups formed via plasma modification of CNPs. Reprinted from Alam et al. [101] with the permission of Elsevier Publishing. CNP: carbon nanoparticle.

Several chemical procedures have been developed to obtain dispersible functionalised graphene. One of the most effective is the covalent attachment of functionalities to pristine graphene) [119]. The main advantage of this method is increasing the dispersibility of graphene sheet in organic solvents which is an important move toward formation of nanocomposite materials with graphene. For instance by functionalization, allows the addition of chromophores, which can help improve conductivity [120]. Covalent bonds can be formed by reaction between free radicals or dienophiles and C=C bond of pristine graphene or between organic functional groups and the oxygen groups of graphene. Figure 26 shows different graphene covalent functionalisation methods.

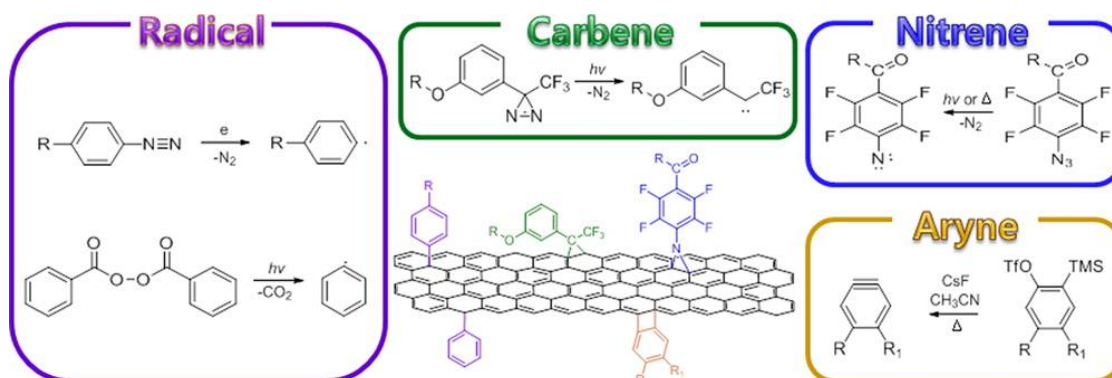


Figure 26. Graphene covalent functionalisation methods. Reprinted from Park et al. [121] with the permission of ACS Publishing. ACS: American Chemical Society.

For example, nitro-phenyls functionalisation of the graphene sheet has been achieved via radical chemistry, Figure 27.

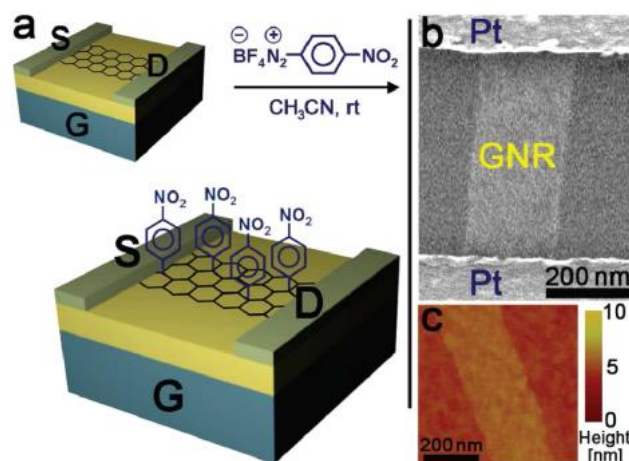


Figure 27. Chemical doping of graphene with 4-nitrophenyl groups: (a) schematic representation; (b) SEM image of a graphene nanoplatelet between Pt electrodes; (c) AFM image of a fragment of a monolayer graphene. Reprinted from Sinitskii et al. [122] with the permission of ACS Publishing. SEM: scanning electron microscopy; ACS: American Chemical Society; AFM: atomic force microscopy.

Another alternative is using carbene precursors to functionalize the graphene sheet [123], Chloroform and diazine as carbene precursors have been used to functionalise graphene oxide.

Nitrenes have also been used in the functionalization of graphene sheet. Graphene sheets were reacted with Boc-protected azidophenylalanine in ODCB. The product was determined to have 1 phenylalanine substituent per 13 carbons (Figure 28).

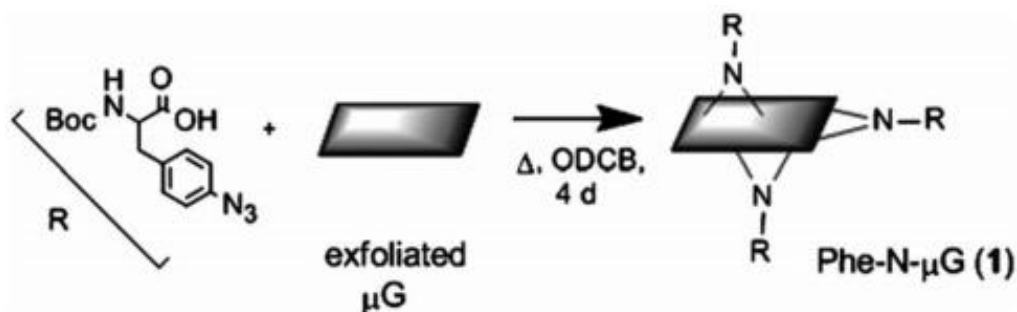


Figure 28. Nitrene addition to graphene sheets using Boc-protected azidophenylalanine. Reprinted from Strom et al. [124] with the permission of RSC Publishing. RSC: Royal Society of chemistry.

In this method, the degree of functionalization is dependent on the amount of nitrene added to the reaction mixture (Figure 29).

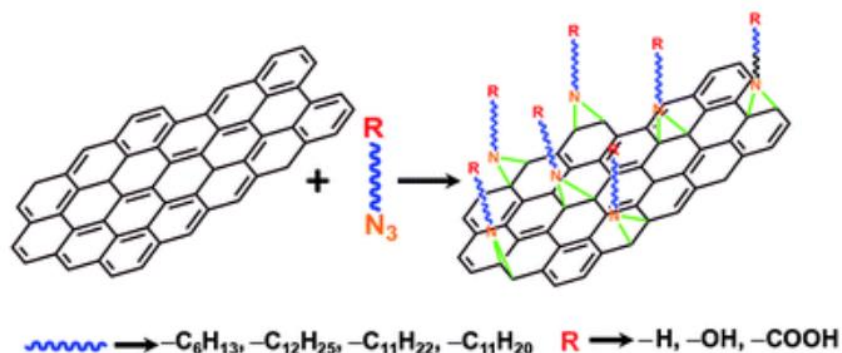


Figure 29. The reaction of alkyl nitrenes with graphene sheets. Reprinted from Vadukumpully et al. [125] with the permission of RSC Publishing. RSC: Royal Society of chemistry.

In general, covalent modification breaks the extended conjugation of π -electrons in graphene, resulting in band gap opening and change in conductivity. Also added functional groups to the surface of the graphene sheet will control the chemical properties of the graphene and allows further conjugation of additional molecules and materials to the graphene; beside that covalent modification can improve their solubility and ability to be processed [121].

4.2. Increasing hardness of sol-gel coating

Increasing the hardness of the coating makes it more durable under the impact loading by the liquid droplet, [59, 38].

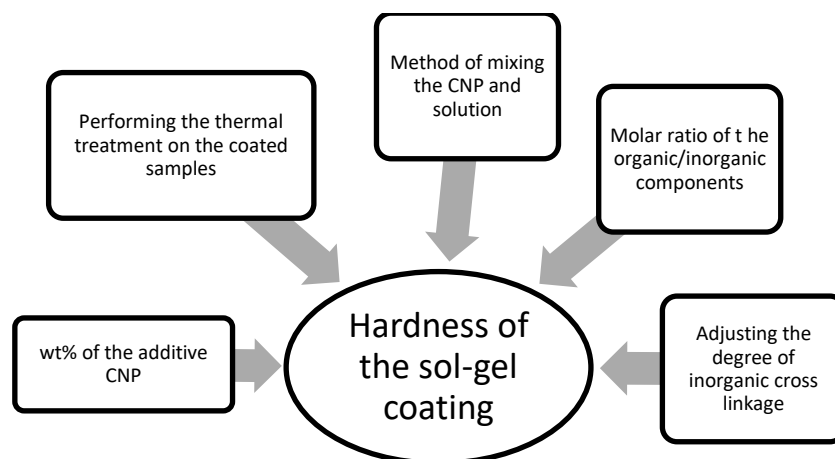


Figure 30. Main parameters that have effect on the hardness of the sol-gel derived coating.

Andrade, et al. [126], provided an economic and convenient inorganic sol-gel route to improve the hardness of the sol-gel coating by adding SWCNTs to the silica matrix. They used water as a precursor of silica and SWCNTs with an average diameter of 1.2 nm and a length of 2-4 μm as a reinforcing agent. In their study, they used pure silica pellets as a reference and prepared composite silica-SWCNTs with 4wt% CNT loading. The microhardness of the pellets was measured using a diamond Vickers indenter with a load of

9.8 N and a dwell-time of 10 sec (at least 10 measurements per samples). The composite and the pure silica showed a microhardness of 600 Hv₁₀₀ and 470 Hv₁₀₀, respectively. UV-Vis and Raman spectroscopy were used to investigate the microstructure of the composites. The Raman spectrum the hybrid CNT-silica film showed a high energy mode (HEM) of SWCNTs around the 1591 cm⁻¹ which proves an interaction between the silica and SWCNTs (Figure 31).

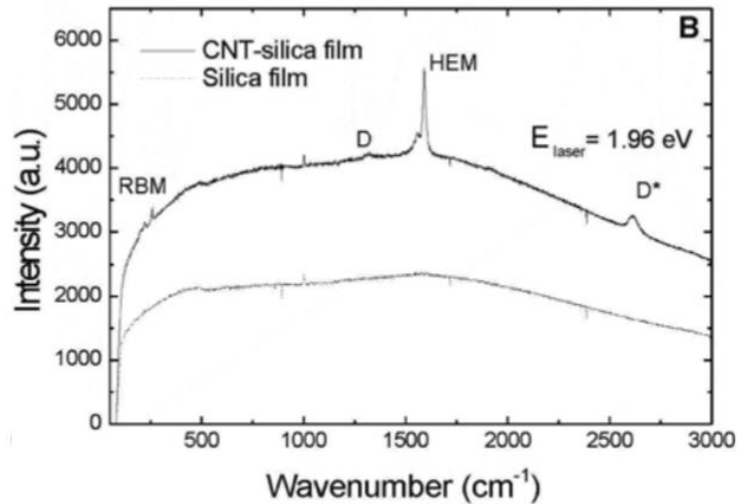


Figure 31. Raman spectroscopy of the Silica-CNTs composite film obtained by dip-coating. Reprinted from Jung de Andrade et al. [126] with the permission of Wiley Inter Science Publishing. CNT: carbon nanotube.

SEM images of the silica-SWCNTs showed an interaction between the silica matrix and SWCNTs as well; they could improve the interfacial stress transfer in the composite and hindered crack propagation because of the effect of crack bridging by SWCNTs.

Lopez, et al. [127] prepared a silica-MWCNTs hybrid coating with a 0.1wt% MWCNT loading. They analyzed the effect of the mixing technique of the sol-gel process on the hardness, fracture toughness and Young's modulus of the hybrid coating. They used the dip coating technique (with a withdrawal speed of 10 cm/min) to deposit the coating on a magnesium alloy substrate. For the characterization purpose, Field Emission Scanning Electron Microscopy (FESEM) and Transmission Electron Microscopy (TEM) for the microstructural observation were performed. Atomic Force Microscopy (AFM) was used to study the morphology and surface roughness. The nano-indentation technique was used to measure the hardness of the coating by applying maximum test loads of 100, 200 and 300 μN . The energy loss during indentation as a result of the coating failure was measured by Bushan's procedure. The coating indentation fracture toughness (K_C) was calculated from the size of the geometry of the residual imprint and the fracture dissipated energy (U_{fr}), using the following equation:

$$K_C = \left(\frac{E_f U_{fr}}{(1-\nu_f^2) A_{fr}} \right)^{1/2} = \left(\frac{E_f U_{fr}}{(1-\nu_f^2) 2\pi C_R} \right)^{1/2} \quad (14)$$

Where E_f and ν_f are the Young's modulus and Poisson's ratio of the coating, respectively, and A_{fr} is the area of the coating which is $2\pi C_R$ and C_R is the length of the cracks developed from the indent edges.

Also the energy associated with coating failure, U_{fr} , can be derived from the difference between the experimental curve and the hypothetical curve which is obtained in absence of failure.

In this study the coatings were fabricated by two mixing methods, mechanically mixing (MM) and ultrasonic mixing (UM). For the UM sol, FEG-SEM showed a different result, Figure 32, for the unreinforced coating at the low magnification the coating seems to be uniform and free of cracks, while at higher magnification small defects are revealed in the flatter zone of the surface. It shows that when the coating is reinforced with MWCNTs an extremely porous microstructure is observed. For the reinforced coating made by UM method there were no free CNTs observed and all the CNTs completely embedded to the coating structure.

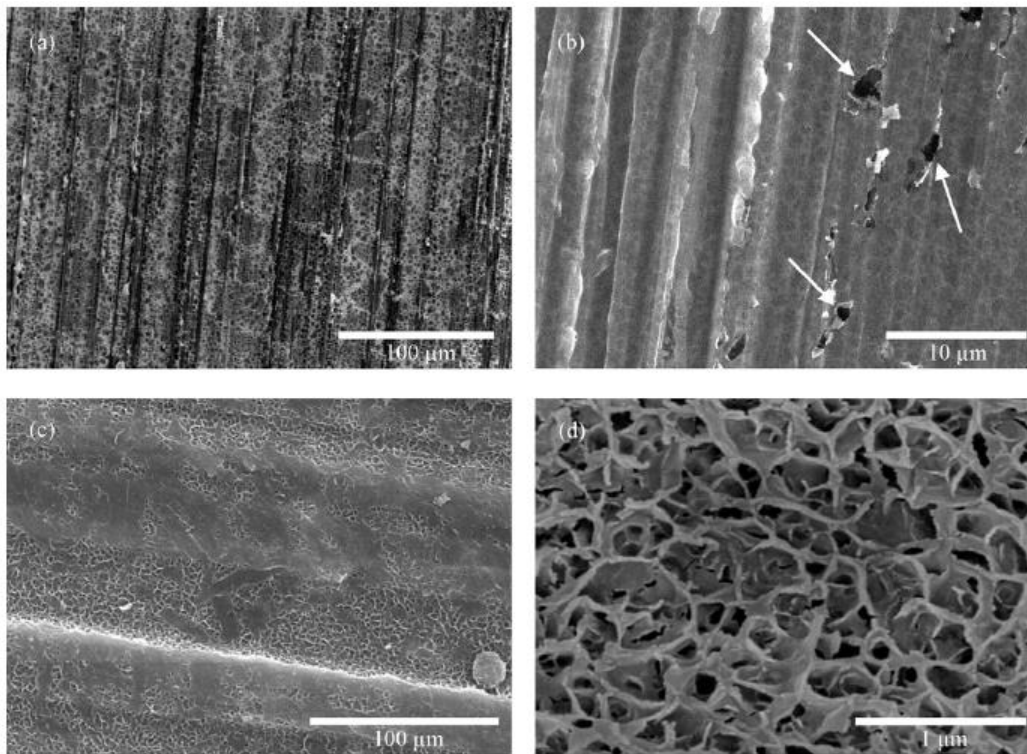


Figure 32. FEG-SEM micrograph of the ultrasonic mixed coatings, unreinforced condition (a) at low magnification, and (b) at high magnification; reinforced condition (c) at low magnification and (d) at high magnification. Reprinted from Lopez et al. [127] with the permission of Elsevier Publishing. FEG-SEM: field emission gun-scanning electron microscopy.

As can be seen in the Table 6 the reinforced ultrasonicated coating (UM+CNTs) was the softest material tested, and the values measured for the MM and MM+CNTs coatings were similar. The results highlight that the inclusion of the carbon nanotube in the sol-gel material by conventional method did not modify in great extent the silica coating properties.

Table 6. Average Young's modulus and hardness of the different tested specimen obtained by nanoindentation [127].

	E (GPa)	H (GPa)
Unreinforced MM	69 ± 4	0.28 ± 0.05
MM+CNT	72 ± 6	0.31 ± 0.06
Unreinforced UM	63 ± 5	0.21 ± 0.04
UM+CNT	42 ± 16	0.11 ± 0.05

MM: mechanically mixing; UM: ultrasonic mixing; CNT: carbon nanotube.

Maeztu, et al. [71] used a multi-layered sol-gel nanocoating to fabricate a new coating on the aluminium with a dual property of hydrophobicity and corrosion resistance. This combination consisted of hybrid sol-gel matrix with a graphene oxide base to provide the corrosion resistance and a simple sol-gel matrix containing fluorinated polymeric chains to provide hydrophobic properties [71]. In their study, they tried to optimise the mechanical properties of the coating by performing thermal treatment (180°C- overnight). After thermal treatment, the hardness of the hybrid coatings was determined using the pencil hardness test. The result of pencil hardness tests revealed that thermal treatment provided a chemical cross-linking between alkoxydes, which increased the hardness of the hybrid coating by a factor of three.

Grundwürmer, et al. [59], tried to enhance the mechanical properties of the sol-gel coating by adding ZrO₂ nanoparticles to the structure of the hybrid sol-gel coating. For this purpose, they developed two types of coatings:

Sol-A, which is glycidoxy propyltrimethoxy silane (GPTMS) and tetraethylorthosilicate (TEOS) and Sol-B, which is GPTMS, aminopropyltriethoxy silane (APTMS), phenyltrimethoxy silane (PTMS) and aluminium-sec-butoxide (AIB) with the ratio of (6.5:0.4:1:2). The hardness of the coatings was measured with Berkovich indenter, the average values of loading-unloading curves of three different maximum loads (300mN, 100mN, 30mN, dwell time: 3S) can be seen in. As a result of hardness measurement, it was found that adding the nanoparticle reinforcement to the coating which has the higher ratio of organic/inorganic components will reduce the hardness of the coating and erosion resistant, as well. Because the high organic content results in limited inorganic cross linking between the nanoparticles and the inorganic part of the sol-gel matrix; however, adding the nanoparticles to the coating with the ratio (1:1) of organic/inorganic component will increase the hardness and erosion resistance of the coating. As can be seen in Figure 33 for the sol-B, adding the nanoparticles decreases the erosion resistance of the coating dramatically, while adding the same nanoparticle to the sol-A with the same ratio of organic/inorganic component will increase the erosion resistant.

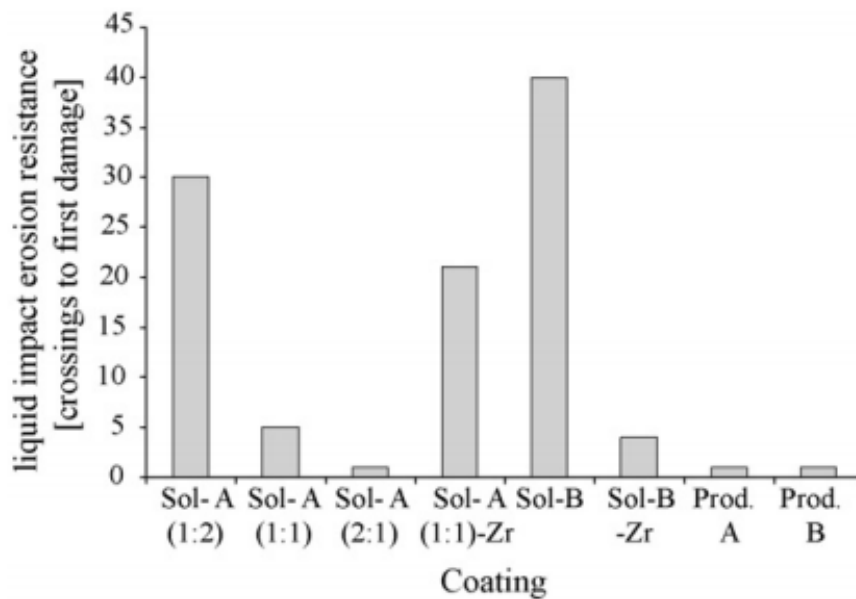


Figure 33. Liquid impact erosion resistance. Reprinted from Grundwürmer et al. [59] with the permission of Elsevier Publishing.

Najafabadi, et al. [38] focused on the optimization of compositional and process parameters of hybrid nanocomposite sol-gel coatings, resistant to rain erosion, by using a statistical design of experimental methodology based on Taguchi orthogonal design. The adhesion (pull-off), flexibility (impact and mandrel bending), hardness (a pencil scratch hardness measurement), wear (Taber wear index) and rain erosion resistance (stationary sample erosion test) of optimized coatings were analyzed. The selected five parameters which have the main effect on the rain erosion resistant properties of the coating are: inorganic/organic molar ratio, hydrolysis water content, drying temperature, curing temperature, and curing time.

As a result of their study, the optimum coating with the highest rain erosion resistant have a GPTMS/TEOS ratio of 3/7, hydrolysis water content of $x=12$, dried at 60°C , and cured at 130°C for 90 minutes. This coating had pencil hardness higher than 6H.

4.3. Increasing the resilience of the sol-gel coating

Resilience is the ability of a coating to absorb energy when it is deformed elastically, and release that energy upon unloading without formation of any cracks or other mode of failures. Higher resilience results in more erosion resistant coating [59].

Grundwürmer, et al. [59] analysed the effect of adding nanoparticle on the resilience of a sol-gel derived coating. In their study, they added ZrO_2 nanoparticles to the hybrid sol-gel coating. The flexibility of the coatings were measured by two different types of tests; impact test (ISO 1519) and mandrel bending test (ISO 1519). The tests are considered as passed when no cracks are observed and the coating remains stuck to the substrate without spalling.

All 6 types of sol-gel coating tested passed the impact test but three of them failed the mandrel test (Sol-A (1:2), Sol-B, Sol-B-Zr), Figure 34.

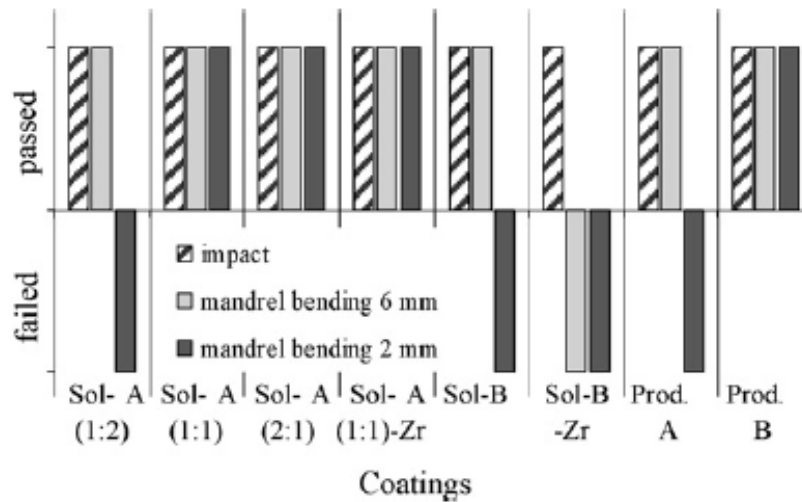


Figure 34. Results from impact and mandrel bending tests. All samples are flexible enough to pass the impact test. Less flexible coating failed the mandrel bending test. Reprinted from Grundwürmer et al. [59] with the permission of Elsevier Publishing.

For all six sol-gel systems, adding nanoparticles showed no negative effect on the flexibility of the coating. Sol-A (1:2) which has a large inorganic/organic ratio, the coating shows less flexibility which means, a lower organic component (GPTMS) increase the degree of cross-linking and reduced resilience (flexibility) of the coating. For the Sol-B having the harder component in its structure (AIB) decreases the flexibility of the coating and that is why it failed at mandrel bending 2mm. However, for the Sol-B-Zr, the addition of a large amount of nanoparticles (30 wt%) to its structure resulted in an increase in the hardness of the coating, causing the coating to fail in the 2mm and 6mm mandrel bending tests.

Najafabadi, et al. [38] optimized the flexibility of a coating by performing impact (ASTM D2794) and mandrel bending (ASTM D522) Tests; their optimum coatings could pass the conical mandrel bending test and 151.15 in-lb impact resistance. A visual examination of the coated substrates showed that there were no cracks or loss of adhesion of the coating in the region of impact or the area of the bend. The results of the tests show that the optimized coating has excellent fracture toughness, and these coatings are very flexible and can withstand the stresses during fabrication. Also the study shows that the optimized coating good rain erosion resistance as it is hard enough to avoid cracks from rain droplet impact and also resilient enough (flexible) to absorb the impulse transferred by the water droplet.

4.4. Increasing the adhesion of the sol-gel coating to the substrate

With the sol-gel techniques, it is possible to manufacture coatings with good adhesion to the substrate. The adhesion can be strengthened through covalent bonding between the sol gel and the surface via condensation with hydroxyl groups or via other linking groups (e.g. amines and epoxides), (Figure 35).

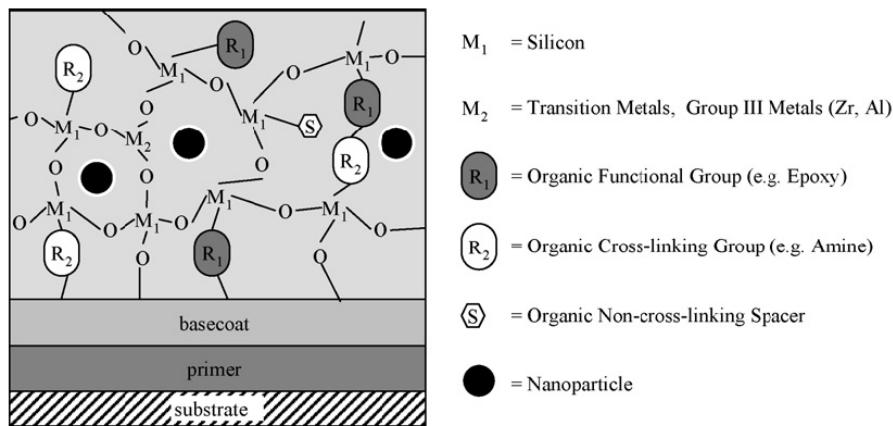


Figure 35. Schematic layer composition of the organic–inorganic hybrid coating reinforced by nanoparticles based on silica. Reprinted from Grundwürmer et al. [59] with the permission of Elsevier Publishing.

Grundwürmer, et al. [59] used ZrO_2 nanoparticle to enhance the adhesion properties of the coating. For this purpose cross cut tests (EN ISO 2409, GT0 = no spalling, GT5 = complete spalling) were performed and the results showed no negative effects on the adhesion properties as a result of adding nanoparticles to the coating (Figure 36).

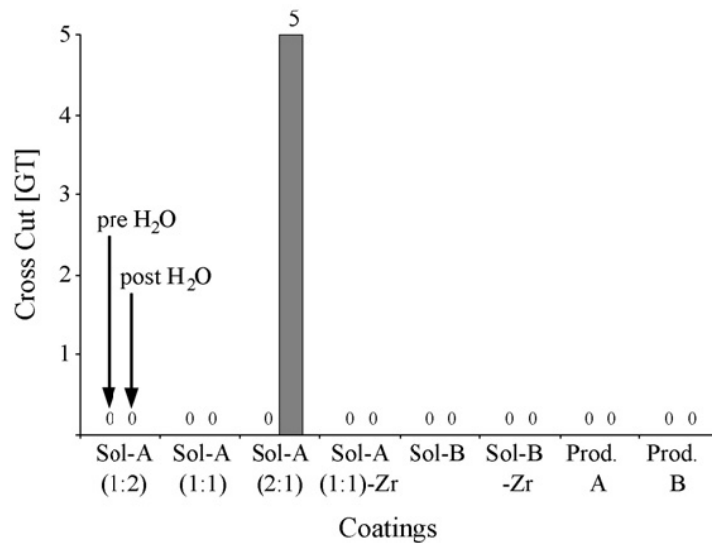


Figure 36. Adhesion measured by cross cut test (ISO 2409, GT 0 = no spalling, GT 5 = complete spalling). The adhesion was measured prior to 14 days water immersion at RT (pre H₂O) and afterwards (post H₂O). Reprinted from Grundwürmer et al. [59] with the permission of Elsevier Publishing.

Najafabadi, et al. [38], tried to optimize the adhesion properties of the sol–gel coating by changing the hydrolysis water content and the ratio of organic/inorganic components in the composite mixture. Adhesion of the coating to the substrate was evaluated by pull-off method. They found that increasing the hydrolysis water content and decreasing the organic content increased the silanol (Si–OH) concentration. This increases the possibility of the formation of Si–O–Al links, and consequently, increasing adhesion of the coating to the substrate.

4.5. Increasing the water contact angle in sol–gel coating

Maeztu, et al. [71] proposed a multi-layered sol–gel nanocoating onto aluminium to fabricate a new surface with a dual property of hydrophobicity and corrosion resistance. This combination consists of hybrid sol–gel matrix which is graphene oxide-based to provide the corrosion resistance and a simple sol–gel matrix which has fluorinated polymeric chains to provide the hydrophobic properties [71]. The surface and coating morphology was analysed by Atomic Force Microscopy (AFM), profilometry and Scanning Electron Microscopy (SEM). The hydrophobicity properties and Water Contact Angle (WCA) were measured and the corrosion resistance was analysed by potentiodynamic polarization and electrochemical impedance spectroscopy.

Table 7 summarizes the WCA for the aluminium substrate coated with two-step layer-by-layer coating (coating 1 and 2) at 6.

The results presented in Table 8 show that the corrosion resistance increases with increasing thickness of the samples (1 to 6 dips). Also the hybrid-coating GPTMS-MTEOS-GrOx-PFAS which was prepared by a two-step layer by layer coating had the lowest amount of pitting corrosion. In addition, it was found that an increase in the WCA correlated with an increase in the corrosion resistance [71].

Table 7. Effects of the two different types of coating, dips and thermal treatment on the water contact angle [71].

Sample	1 st Coating	No of Dips	2 nd Coating	Dips	Thermal Treatment	WCA
1	Aluminium bare substrate					17.14 ⁰
2	GPTMS-MTEOS-GrOx	1				24.37 ⁰
3	PFAS	1				87.35 ⁰
4	GPTMS-MTEOS-GrOx	1	PFAS	1		95.31 ⁰
5	GPTMS-MTEOS-GrOx	1	PFAS	1	Done	107.23 ⁰
6	GPTMS-MTEOS-GrOx	6				36.24 ⁰
7	PFAS	6				107.04 ⁰
8	GPTMS-MTEOS-GrOx	6	PFAS	6		107.23 ⁰
9	GPTMS-MTEOS-GrOx	6	PFAS	6	Done	124.87 ⁰

GPTMS: glycidoxy propyltrimethoxy silane; WCA: water contact angle; PFAS: perfluorooctyltriethoxysilane.

Table 8. Pitting corrosion as a function of the number of dips and thermal treatment [71].

Samples	1 st Coating	Dips	2 nd Coating	Dips	Thermal treatment	Potential Pitting corrosion
1	Aluminium bare substrate					-570mV
2	GPTMS-MTEOS	1				-540mV
3	GPTMS-MTEOS	6				-520mV
4	GPTMS-MTEOS-GrOx	1				-520mV
5	GPTMS-MTEOS-GrOx	6				-330mV
6	PFAS	1				-500mV
7	PFAS	6				-420mV
8	GPTMS-MTEOS-GrOx	1	PFAS	1	Done	-420mV
9	GPTMS-MTEOS-GrOx	6	PFAS	6	Done	-280mV

GPTMS: glycidoxy propyltrimethoxy silane; PFAS: perfluorooctyltriethoxysilane.

5. Conclusion

The development of rain erosion coating for wind turbine blades requires tools for erosion lifetime prediction and identification of suitable combination of coating and composite substrate. It has been shown that protecting the leading edge (LE) of wind turbine blade against rain erosion is very important for making wind turbine energy production cost competitive. An overview of the liquid impact phenomena allowing one to identify how adhesion and erosion are affected by the shock wave caused by the collapsing water droplet on impact are discussed. It is reported that eroded blades can reduce the annual energy production (AEP) of the wind turbine by 20-25%. Coating the blade against erosion using appropriate materials substantially reduces these losses and it is more economical to protect the blades from environmental erosion than repair or replace them.

The emphasis was on the sol-gel coatings for LE of wind turbine and their advantages and drawbacks are discussed; methods of depositing the sol-gel derived coating on the substrate and improving the mechanical properties of the coating by using carbon nanoparticles (CNPs) in the structure of sol-gel are reviewed.

A sol-gel derived coating typically has a maximum thickness of the 10 μ m which has a negligible effect on the weight of the blade. A sol-gel coating with increasing the hydrolysis water content, hardness and flexibility plus decreasing the organic/inorganic molar ratio will increase the rain erosion resistant. On the other hand, poor adhesion of the coating to the substrate will decrease the rain erosion resistant.

Various studies showed that addition of carbon nanoparticles (CNPs), especially carbon nanotubes and graphenes, in the structure of the coating greatly enhances the erosion

resistant of the coating. However, proper functionalisation of CNPs is required for effective dispersion which positively affects the properties of the coating.

Rain erosion durability testing of the coatings through accelerated rain erosion testing was discussed. Establishing the incubation time of the erosion damage is required from the rain erosion tests. The mechanical testing involved for establishing a suitable coating includes pull-off testing, peeling–adhesion testing and nanoindentation testing of the coating. In order to understand the details of erosion process and characterise the failure mechanism, numerical models of rain droplet impact simulations are necessary.

5.1. Prospect of new development of erosion resistance coating

At the moment there are different types of the erosion protection systems which are used to protect the wind turbine blades against environmental effects, such as tapes, paintable coatings and vacuum techniques like chemical vapour deposition. It is desirable to develop a new generation of coatings which are cost effective, durable and easy to apply. The new coating should have additional advantages over the existing coatings, such as:

- Thin layer coating: having negligible effects on the weight of the blades.
- Multifunctional properties: resistant to erosion, corrosion, abrasion, de–icing and having flexibility at the same time.
- Lower temperature required for curing process: the coating should be able to be cured at room temperature or low temperature to reduce the energy consumption of the curing process.
- Environmental friendly: can be achieved by using organic compounds in the structure of the coating.
- Desirable mechanical properties: High tensile strength and flexibility, good adhesion to the substrate and having stable chemical properties which can be achieved by using CNPs in the structure of the coating.

The sol–gel technique has the potential for development of coatings with the above characteristics.

References

- [1] S. Somani and H. Koenig, KPMG, [Online]. Available: <https://home.kpmg.com/content/dam/kpmg/sg/pdf/2016/11/Global-Trends-in-Renewable-Energy.pdf>. [Accessed 04 09 2018].
- [2] D. Li, S. M. Ho, G. Song, L. Ren and H. Li, "A review of damage detection methods for wind turbine blades," *Smart Materials and Structures*, vol. 24, no. 3, p. 033001, 2015.
- [3] G. Fiore and M. Selig, "Simulation of Damage Progression on Wind Turbine Blades," in *American Institute of Aeronautics and Astronautics*, California, 2016.
- [4] C. Ciang, J. Lee and H. Bang, "Structural health monitoring for a wind turbine system: a review of damage detection methods," *Measurement Science and Technology*, vol. 19, no. 12, p. 122001, 2008.
- [5] F. Larsen and T. Sorensen, "New lightning qualification test procedure for large wind turbine blades," in *International Conference on Lightning and Static Electricity (ICLOSE)*, Blackpool, Blackpool, 2003.
- [6] M. H. Keegan, D. H. Nash and M. M. Stack, "On erosion issues associated with the leading edge of wind turbine blades," *J. Phys. D: Appl. Phys.*, vol. 46, no. 38, p. 383001, 2013.
- [7] H. J. Sutherland, "A summary of the fatigue properties of wind turbine materials," *Wind Energy*, vol. 3, no. 1, pp. 1-34, 2000.
- [8] J. Martino, "Power-eng.com," 14 03 2014. [Online]. Available: <http://www.power-eng.com/articles/print/volume-118/issue-3/features/advancements-in-wind-turbine-technology-improving-efficiency-and-reducing-cost.html>. [Accessed 12 12 2017].
- [9] P. Brøndsted, H. Lilholt and A. Lystrup, "Composite materials for wind power turbine blades," *Annual Review of Materials Research*, vol. 35, no. 1, pp. 505-538, 2005.
- [10] O. Al-Khudairi, H. Hadavinia, C. Little, G. Gillmore, P. Greaves and K. Dyer, "Full-scale fatigue testing of a wind turbine blade in flapwise direction and examining the effect of crack propagation on the blade performance," *Materials*, vol. 10, no. 10, p. 1152, 2017.
- [11] M. A. S. Shohag, E. C. Hammel, D. O. Olawale and O. I. Okoli, "Damage mitigation techniques in wind turbine blades: A review," *Wind Engineering*, vol. 41, no. 3, pp. 185-210, 2017.

- [12] L. Mishnaevsky, K. Branner, H. Petersen, J. Beauson, M. Mcgugan and B. Sgrensen, "Materials for Wind Turbine Blades: An Overview," *Materials*, vol. 10, no. 11, p. 1285, 2017.
- [13] M. Schramm, H. Rahimi, B. Stoevesandt and K. Tangager, "The Influence of Eroded Blades on Wind Turbine Performance Using Numerical Simulations," *Energies*, vol. 10, no. 9, p. 1420, 2017.
- [14] W. Han, J. Kim and B. Kim, "Effects of contamination and erosion at the leading edge of blade tip airfoils on the annual energy production of wind turbines," *Renewable Energy*, vol. 115, pp. 817-823, 2018.
- [15] A. Sareen, C. A. Sapre and M. S. Selig, "Effects of leading edge erosion on wind turbine blade performance," *Wind Energy*, vol. 17, no. 10, pp. 1531-1542, 2013.
- [16] E. Cortés, F. Sánchez, A. O'Carroll, B. Madramany, M. Hardiman and T. M. Young, "On the material characterisation of wind turbine blade coatings: the effect of interphase coating–laminate adhesion on rain erosion performance," *Materials*, vol. 10, p. 1146, 2017.
- [17] S. Zhang, K. Dam-Johansen, S. Nørkjær, P. L. Bernad and S. Kiil, "Erosion of wind turbine blade coatings – Design and analysis of jet-based laboratory equipment for performance evaluation," *Progress in Organic Coatings*, vol. 78, pp. 103-115, 2015.
- [18] Y. Oka and H. Miyata, "Erosion behaviour of ceramic bulk and coating materials caused by water droplet impingement," *Wear*, vol. 267, no. 11, pp. 1804-1810, 2009.
- [19] C. Alessio, "Computational analysis of wind-turbine blade rain erosion," *Computers & Fluids*, vol. 141, pp. 175-183, 2016.
- [20] S. Zhang, K. Dam-Johansen, P. L. Bernad and S. Kiil, "Rain erosion of wind turbine blade coatings using discrete water jets: Effects of water cushioning, substrate geometry, impact distance, and coating properties," *Wear*, Vols. 328-329, pp. 140-148, 2015.
- [21] Sun & Wind Energy, "Eradicating blade damage (Nov. 2014)," 17 Nov 2014. [Online]. Available: <http://www.sunwindenergy.com/wind-energy/eradicating-blade-damage>. [Accessed 02 01 2019].
- [22] L. Rempel, "Rotor blade leading edge erosion real life experiences," *Wind Systems Mag*, Oct. 2012.
- [23] A. O'Carroll, M. Hardiman, E. F. Tobin and T. M. Young, "Correlation of the rain erosion performance of polymers to mechanical and surface properties measured using nanoindentation," *Wear*, Vols. 412-413, pp. 38-48, 2018.

- [24] R. Kithil, "Lightningsafety.com," National Lightning Safety Institute, 6 2008. [Online]. Available: http://www.lightningsafety.com/nlsi_lhm/wind_blade_damage.pdf. [Accessed 12 1 2018].
- [25] A. Fraisse, J. I. Bech, K. K. Borum, V. Fedorov, J. N. F-J, M. McGugan, L. Mishnaevsky and Y. Kusano, "Impact fatigue damage of coated glass fibre reinforced polymer laminate Fraisse," *Renewable Energy*, vol. 126, pp. 1102-1112, 2018.
- [26] Y. Kusano, V. Fedorov, M. McGugan, T. L. Andersen and N. F.-J. Johansen, "Impact damage reduction by structured surface geometry," *Materials Letters*, vol. 221, pp. 296-300, 2018.
- [27] P. Panagos, C. Ballabio, P. Borrelli and et al., "Rainfall erosivity in Europe," *Science of the Total Environment*, vol. 511, pp. 801-814, 2015.
- [28] P. Panagos, P. Borrelli, K. Meusburger and et al., "Global rainfall erosivity assessment based on high-temporal resolution rainfall records," *Scientific Reports*, vol. 7, p. Article number: 4175, 2017.
- [29] J. I. Bech, C. B. Hasager and C. Bak, "Extending the life of wind turbine blade leading edges by reducing the tip speed during extreme precipitation events," *Wind Energ. Sci.*, vol. 3, pp. 729-748, 2018.
- [30] B. Amirzadeh, A. Louhghalam, M. Raessi and M. Tootkaboni, "A computational framework for the analysis of rain-induced erosion in wind turbine blades, part I: Stochastic rain texture model and drop impact simulations," *J. Wind Eng. Ind. Aerodyn.*, vol. 163, pp. 33-43, 2017.
- [31] B. Amirzadeh, A. Louhghalam, M. Raessi and M. Tootkaboni, "A computational framework for the analysis of rain-induced erosion in wind turbine blades, part II: Drop impact-induced stresses and blade coating fatigue life," *J. Wind Eng. Ind. Aerodyn.*, vol. 163, pp. 44-54, 2017.
- [32] N. Fujisawa, T. Yamagata, K. Hayashi and T. Takano, "Experiments on liquid droplet impingement erosion by high-speed spray," *Nuclear Engineering and Design*, vol. 250, pp. 101-107, 2012.
- [33] N. Fujisawa, T. Yamagata and K. Wada, "Attenuation of wall-thinning rate in deep erosion by liquid droplet impingement," *Annals of Nuclear Energy*, vol. 88, pp. 151-157, 2016.
- [34] N. Fujisawa, T. Yamagata, S. Takano, K. Saito, R. Morita, K. Fujiwara and F. Inada, "The influence of material hardness on liquid droplet impingement erosion," *Nuclear Engineering and Design*, vol. 288, pp. 27-34, 2015.

- [35] N. Fujisawa, T. Yamagata, K. Saito and K. Hayashi, "The effect of liquid film on liquid droplet impingement erosion," *Nuclear Engineering and Design*, vol. 265, pp. 909-917, 2013.
- [36] F. Heymann, "Liquid impingement erosion," in *Friction, Lubrication, and Wear Technology*, vol. 18, ASM International, 1992, pp. 221 - 231.
- [37] Y. Oka, S. Mihara and H. Miyata, "Effective parameters for erosion caused by water droplet impingement and applications to surface treatment technology," *Wear*, vol. 263, no. 1-6, pp. 386-394, 2007.
- [38] A. Hojjati Najafabadi, R. Shoja Razavi, R. Mozaffarinia and H. Rahimi, "A New Approach of Improving Rain Erosion Resistance of Nanocomposite Sol-Gel Coatings by Optimization Process Factors," *Metallurgical and Materials Transactions A*, vol. 45, no. 5, pp. 2522-2531, 2014.
- [39] B. Lee, K. Riu, S. Shin and S. Kwon, "Development of a water droplet erosion model for large steam turbine blades," *KSME International Journal*, vol. 17, no. 1, pp. 114-121, 2003.
- [40] S. DeCorso, "Erosion tests of steam turbine blade materials.," *American Society for Testing and Materials - Proceedings*, vol. 64, pp. 782-796, 1964.
- [41] M. J. Jackson and J. E. Field, "Modelling liquid impact fracture thresholds in brittle materials," *British Ceramic Transactions*, vol. 99, pp. 1-13, 2000.
- [42] M. B. Lesser and J. E. Field, "The Impact of Compressible Liquids," *Annual Review of Fluid Mechanics*, vol. 15, no. 1, pp. 97-122, 1983.
- [43] P. Shipway and K. Gupta, "The potential of WC-Co hardmetals and HVOF sprayed coatings to combat water-droplet erosion," *Wear*, vol. 271, no. 9-10, pp. 1418-1425, 2011.
- [44] J. Zahavi and S. Nadiv, "Indirect damage in composite materials due to raindrop impact," *Wear*, vol. 72, pp. 305-313, 1981.
- [45] R. J. Wasley, *Stress wave propagation in solids, an introduction.*, New York: M. Dekker, 1973.
- [46] H. Slot, E. Gelinck, C. Rentrop and E. van der Heide, "Leading edge erosion of coated wind turbine blades: Review of coating life models," *Renewable Energy*, vol. 80, pp. 837-848, 2015.
- [47] E. Tobin, T. Young, D. Raps and O. Rohr, "Comparison of liquid impingement results from whirling arm and water-jet rain erosion test facilities," *Wear*, vol. 271, no. 9-10, pp. 2625-2631, 2011.

- [48] E. Tobin, T. Young and D. Raps, "Evaluation and correlation of interlaboratory results from rain erosion test campaign," in *28th Congress of the International Council of Aeronautical Sciences (ICAS)*, Brisbane, Australia, Sep 2012.
- [49] O. Gohardani, "Impact of erosion testing aspects on current and future flight conditions," *Prog. Aerosp. Sci.*, vol. 47, pp. 280-303, 2011.
- [50] R. A. Caruso and M. Antonietti, "Sol–Gel Nanocoating: An Approach to the Preparation of Structured Materials," *Chemistry of Materials*, vol. 13, no. 10, pp. 3272-3282, 2001.
- [51] R. Karmouch and G. G. Ross, "Superhydrophobic wind turbine blade surfaces obtained by a simple deposition of silica nanoparticles embedded in epoxy," *Applied Surface Science*, vol. 257, no. 3, pp. 665-669, 2010.
- [52] C. Peng, S. Xing, Z. Yuan, J. Xiao, C. Wang and J. Zeng, "Preparation and anti-icing of superhydrophobic PVDF coating on a wind turbine blade," *Applied Surface Science*, vol. 259, pp. 764-768, 2012.
- [53] T. Obara, N. Bourne and J. Field, "Liquid-jet impact on liquid and solid surfaces," *Wear*, Vols. 186-187, pp. 388-394, 1995.
- [54] W. F. Adler, "Rain impact retrospective and vision for the future," *Wear*, Vols. 233-235, pp. 25-38, 1999.
- [55] T. Ikohagi, "On Evaluation of LDI Erosion Rate based on Fluid/Solid Coupled Simulation," in *Eighth International Conference on Flow Dynamics*, Sendai, January 2011.
- [56] S. Hattori and M. Kakuichi, "Effect of impact angle on liquid droplet impingement erosion," *Wear*, Vols. 298-299, pp. 1-7, 2013.
- [57] F. J. Heymann, "Conclusions from the ASTM interlaboratory test program with liquid impact erosion facilities," in *Proc. 5th Int. Conf. Erosion by Liquid and Solid Impact*, Cambridge, UK, Sep. 3-6, 1979.
- [58] L. Claire, G. Marie, G. Julien, S. Jean-Michel, R. Jean, M. Marie-Joëlle, R. Stefano and F. Michele, "New architected hybrid sol-gel coatings for wear and corrosion protection of low-carbon steel," *Progress in Organic Coatings*, vol. 99, pp. 337-345, 2016.
- [59] M. Grundwürmer, O. Nuyken, M. Meyer, J. Wehr and N. Schupp, "Sol–gel derived erosion protection coatings against damage caused by liquid impact," *Wear*, vol. 263, no. 1-6, pp. 318-329, 2007.

- [60] B. C. Dave, X. Hu, Y. Devaraj and S. K. Shirshak K. Dhali, "Sol–Gel-Derived Corrosion-Protection Coatings," *Journal of Sol-Gel Science and Technology*, vol. 32, pp. 143-147, 2004.
- [61] G. Y. Richardson, C. S. Lei and W. Tabakoff, "Erosion Testing of Coatings for V-22 Aircraft Applications," *International Journal of Rotating Machinery*, vol. 9, no. 1, pp. 35-40, 2003.
- [62] H. Huang, B. Orlor and G. Wilkes, "Ceramers-hybrid materials incorporating polymeric oligomeric species into inorganic glasses utilizing a sol-gel approach," *Polymer Bulletin*, vol. 14, no. 6, pp. 557-564, 1985.
- [63] H. Schmidt and H. Wolter, "Organically modified ceramics and their applications," *Journal of Non-Crystalline Solids*, vol. 121, no. 1-3, pp. 428-435, 1990.
- [64] K.-H. Haas and H. Wolter, "Synthesis, properties and applications of inorganic–organic copolymers (ORMOCER®s)," *Current Opinion in Solid State and Materials Science*, vol. 4, no. 6, pp. 571-580, 1999.
- [65] S. Dash, S. Mishra, S. Patel and B. K. Mishra, "Organically modified silica: Synthesis and applications due to its surface interaction with organic molecules," *Advances in Colloid and Interface Science*, vol. 140, no. 2, pp. 77-94, 2008.
- [66] L. Sowntharya and R. Subasri, "A comparative study of different curing techniques for SiO₂–TiO₂ hybrid coatings on polycarbonate," *Ceramics International*, vol. 39, no. 4, pp. 4689-4693, 2013.
- [67] R. S. Kalidindi and R. . Subasri, "Sol-gel nanocomposite hard coatings," in *Anti-Abrasive Nanocoatings: Current and Future Applications*, Elsevier, 2015, pp. 105-136.
- [68] T. Olding, M. Sayer and D. Barrow, "Ceramic sol–gel composite coatings for electrical insulation," *Thin Solid Films*, vol. 398–399, pp. 581-586, 2001.
- [69] "Introduction to sol-gel," 2006. [Online]. Available: <http://www.ceramics.mmat.ubc.ca/introduction.html>. [Accessed 1 11 2017].
- [70] V. Gavalas, R. Andrews, D. Bhattacharyya and L. Bachas, "Carbon Nanotube Sol–Gel Composite Materials," *Nano Letters*, vol. 1, no. 12, pp. 719-721, 2001.
- [71] J. D. Maeztu, P. J. Rivero, C. Berlanga, D. M. Bastidas, J. F. Palacio and R. Rodriguez, "Effect of graphene oxide and fluorinated polymeric chains incorporated in a multilayered sol-gel nanocoating for the design of corrosion resistant and hydrophobic surfaces," *Applied Surface Science*, vol. 419, pp. 138-149, 2017.

- [72] S. Attia, J. Wang and J. Shen, "Review on sol-Gel Derived Coatings: Process, Techniques and Optical Applications," *Journal of Materials Science and Technology*, vol. 18, no. 3, pp. 211-218, 2002.
- [73] G. Kickelbick, *Hybrid Materials: Synthesis, Characterization, and Applications, USA: Willey-VCH*, 2007.
- [74] K. Sugiyama, S. Nakahama, S. Hattori and K. Nakano, "Slurry wear and cavitation erosion of thermal-sprayed cermets," *Wear*, vol. 258, no. 5-6, pp. 768-775, 2005.
- [75] D. Meyerhofer, "Characteristics of resist films produced by spinning," *Journal of Applied Physics*, vol. 49, p. 3993, 1978.
- [76] D. E. Bornside, C. W. Macosko and L. E. Scriven, "Spin Coating of a PMMA/Chlorobenzene Solution," *J. Electrochem. Soc.*, vol. 138, no. 1, pp. 317-320, 1991.
- [77] D. B. Hall, P. Underhill and J. M. Torkelson, "Spin coating of thin and ultrathin polymer films," *Polymer Engineering and Science*, vol. 38, no. 12, p. 2039, 1998.
- [78] W. Dou, P. Wang, D. Zhang and J. Yu, "An efficient way to prepare hydrophobic antireflective SiO₂ film by sol-gel method," *Materials Letters*, vol. 167, pp. 69-72, 2016.
- [79] S. Amiri and A. Rahimi, "Hybrid nanocomposite coating by sol-gel method: a review," *Iranian Polymer Journal*, vol. 25, no. 6, pp. 559-577, 2016.
- [80] H. Schmidt., E. Geiter., M. Mennig., H. Krug., C. Becker. and R.-P. Winkler., "The Sol-Gel Process for Nano-Technologies: New Nanocomposites with Interesting Optical and Mechanical Properties," *Sol-Gel Science and Technology*, vol. 13, no. 1-3, p. 397-404, 1998.
- [81] M. Aegerter, "Characterization of the mechanical properties of sol-gel coatings," in *Sol-Gel Science and Technology*, Springer, Cham, 2017, pp. 1-19.
- [82] C. Marzolin, A. Terfort, J. Tien and G. M. Whitesides, "Patterning of a polysiloxane precursor to silicate glasses by microcontact printing," *Thin Solid Films*, vol. 315, no. 1-2, pp. 9-12, 1998.
- [83] D. Rickerby, "A review of the methods for the measurement of coating-substrate adhesion," *Surface and Coatings Technology*, vol. 36, no. 1-2, pp. 541-557, 1988.
- [84] ASTM D3359-02, "Standard Test Methods for Measuring Adhesion by Tape Test." West Conshohocken 2002.

- [85] L. Sowntharya, S. Lavanya, G. R. Chandra, N. Hebalkar and R. Subasri, "Investigations on the mechanical properties of hybrid nanocomposite hard coatings on polycarbonate," *Ceramics International*, vol. 38, no. 5, pp. 4221-4228, 2012.
- [86] N. Asadi, R. Naderi and M. Saremi, "Effect of Curing Conditions on the Protective Performance of an Ecofriendly Hybrid Silane Sol–Gel Coating with Clay Nanoparticles Applied on Mild Steel," *Industrial & Engineering Chemistry Research*, vol. 53, no. 26, pp. 10644-10652, 2014.
- [87] M. Ketonen, "UV curing of hybrid coatings,," Tampere University of Applied Sciences, 2011.
- [88] M. Çakır, "Investigation of Coating Performance of UV-Curable Hybrid Polymers Containing 1H,1H,2H,2H-Perfluorooctyltriethoxysilane Coated on Aluminum Substrates," *Coatings*, vol. 7, no. 3, p. 37, 2017.
- [89] N. Domun, H. Hadavinia, T. Zhang, T. Sainsbury, G. H. Liaghat and S. Vahid, "Improving fracture toughness and strength of epoxy using nanomaterials – A review of current status," *Nanoscale*, vol. 7, no. 23, p. 10294–10329, 2015.
- [90] M. Goosey, "A short introduction to graphene and its potential interconnect applications," *Circuit World*, vol. 38, no. 2, pp. 83-86, 2012.
- [91] R. Maria-Hormigos, B. Jurado-Sanchez and L. Vazquez, "Carbon Allotrope Nanomaterials Based Catalytic Micromotors," *Chemistry of Materials*, vol. 28, no. 24, pp. 8962-8970, 2016.
- [92] S. Iijima and T. Ichihashi, "Single-shell carbon nanotubes of 1-nm diameter," *Nature*, vol. 363, pp. 603-605, 1993.
- [93] S. Iijima, "Helical microtubules of graphitic carbon," *Nature*, vol. 354, no. 6348, pp. 56-58, 1991.
- [94] A. Eatemadi, H. Daraee, H. Karimkhanloo, M. Kouhi, N. Zarghami, A. Akbarzadeh, M. Abasi, Y. Hanifehpour and S. Joo, "Carbon nanotubes: properties, synthesis, purification, and medical applications," *Nanoscale Research Letters*, vol. 9, no. 1, p. 393, 2014.
- [95] H. Dai, "Carbon Nanotubes: Synthesis, Integration, and Properties," *Accounts of Chemical Research*, vol. 35, no. 12, pp. 1035-1044, 2002.
- [96] M. Dresselhaus, G. Dresselhaus and R. C. Saito, "Physics of carbon nanotubes," vol. 33, no. 7, pp. 883-891, 1995.
- [97] S. Kushch and N. Kuyunko, "Fullerene black: Structure, properties and possible applications," *Russian Journal of General Chemistry*, vol. 81, no. 2, pp. 345-353, 2011.

- [98] A. Castro Neto, F. Guinea, N. Peres, K. Novoselov and A. Geim, "The electronic properties of graphene," *Reviews of Modern Physics*, vol. 81, no. 1, pp. 109-162, 2009.
- [99] S. Chatterjee, F. A. Nuesch and B. T. T. Chu, "Comparing carbon nanotubes and graphene nanoplatelets as reinforcements in polyamide 12 composites," *Nanotechnology*, vol. 22, no. 27, p. 275714, 2011.
- [100] I. D. Rosca, F. Watari, M. Uo and T. Akasaka, "Oxidation of multiwalled carbon nanotubes by nitric acid," *Carbon*, vol. 43, no. 15, pp. 3124-3131, 2005.
- [101] A. Alam, C. Wana and T. McNally, "Surface amination of carbon nanoparticles for modification of epoxy resins: plasma-treatment vs. wet-chemistry approach," *European Polymer Journal*, vol. 87, pp. 422-448, 2017.
- [102] X.-Z. Tang, W. Li, Z.-Z. Yu, M. A. Rafiee, J. Rafiee, F. Yavari and N. Koratkar, "Enhanced thermal stability in graphene oxide covalently functionalized with 2-amino-4,6-didodecylamino-1,3,5-triazine," *Carbon*, vol. 49, no. 4, pp. 1258-1265, 2011.
- [103] Q. Zhang, J. Wu, L. Gao, T. Liu, W. Zhong, G. Sui, G. Zheng, W. Fang and X. Yang, "Dispersion stability of functionalized MWCNT in the epoxy-amine system and its effects on mechanical and interfacial properties of carbon fiber composites," *Materials & Design*, vol. 94, pp. 392-402, 2016.
- [104] K. A. Wepasnick, B. A. Smith, K. E. Schrote, H. K. Wilson, S. R. Diegelmann and D. H. Fairbrother, "Surface and structural characterization of multi-walled carbon nanotubes following different oxidative treatments," *Carbon*, vol. 49, no. 1, pp. 24-36, 2011.
- [105] B. Smith, K. Wepasnick, K. E. Schrote, H. Cho, W. P. Ball and D. H. Fairbrother, "Influence of Surface Oxides on the Colloidal Stability of Multi-Walled Carbon Nanotubes: A Structure-Property Relationship," *Langmuir*, vol. 25, no. 17, pp. 9767-9776, 2009.
- [106] N. Domun, K. Paton, H. Hadavinia, T. Sainsbury, T. Zhang and H. Mohamud, "Enhancement of Fracture Toughness of Epoxy Nanocomposites by Combining Nanotubes and Nanosheets as Fillers," *Materials*, vol. 10, no. 12, p. 1179, 2017.
- [107] H. Hiura, T. W. Ebbesen and K. Tanigaki, "Opening and purification of carbon nanotubes in high yields," *Advanced Materials*, vol. 7, no. 3, pp. 275-276, 1995.
- [108] N. Blanchard, R. Hatton and S. Silva, "Tuning the work function of surface oxidised multi-wall carbon nanotubes via cation exchange," *Chemical Physics Letters*, vol. 434, no. 1-3, pp. 92-95, 2007.

- [109] N. Montakhab, S. Sadegh Hassani, A. Rashidi and H. Arabi, "Synthesis and characterization of SiO₂-CNT hybrid using sol-gel method," in *Ultrafine Grained and Nanostructured Materials*, Tehran, 2011.
- [110] Y. Peng and H. Liu, "Effects of Oxidation by Hydrogen Peroxide on the Structures of Multiwalled Carbon Nanotubes," *Industrial & Engineering Chemistry Research*, vol. 45, no. 19, pp. 6483-6488, 2006.
- [111] K. J. Ziegler, Z. Gu, J. Shaver, Z. Chen, E. L. Flor, D. J. Schmidt, C. Chan, R. H. Hauge and R. E. Smalley, "Cutting single-walled carbon nanotubes," *Nanotechnology*, vol. 16, no. 7, pp. 539-544, 2005.
- [112] J. Shen, W. Huang, L. Wu, Y. Hu and M. Ye, "Study on amino-functionalized multiwalled carbon nanotubes," *Materials Science and Engineering: A*, vol. 464, no. 1-2, pp. 151-156, 2007.
- [113] W. Wu, C. Wan and Y. Zhang, "Graphene oxide as a covalent-crosslinking agent for EVM-g-PA6 thermoplastic elastomeric nanocomposites," *RSC Advances*, vol. 5, no. 49, p. 39042-39051, 2015.
- [114] W. Zhao, M. Fang, F. Wu, H. Wu, L. Wang and C. G., "Preparation of graphene by exfoliation of graphite using wet ball milling," *Journal of Materials Chemistry*, vol. 20, no. 28, pp. 5817-581, 2010.
- [115] N. Pierard, A. Fonseca, Z. Konya, I. Willems, G. Van Tendeloo and J. B. Nagy, "Production of short carbon nanotubes with open tips by ball milling," *Chemical Physics Letters*, vol. 335, no. 1-2, pp. 1-8, 2001.
- [116] I.-Y. Jeon, H.-J. Choi, S.-M. Jung, J.-M. Seo, M.-J. Kim, L. Dai and J.-B. Baek, "Large-scale production of edge-selectively functionalized graphene nanoplatelets via ball milling and their use as metal-free electrocatalysts for oxygen reduction reaction," *Journal of the American Chemical Society*, vol. 135, no. 4, pp. 1386-1393, 2013.
- [117] R. d'Agostino, P. Favia, C. Oehr and M. Wertheimer, "Low-temperature plasma processing of materials: past, present, and future," *Plasma Processes and Polymers*, vol. 2, no. 1, pp. 7-15, 2005.
- [118] T. Desmet, R. Morent, N. D. Geyter, C. Leys, E. Schacht and P. Dubruel, "Nonthermal plasma technology as a versatile strategy for polymeric biomaterials surface modification: a review," *Biomacromolecules*, vol. 10, no. 9, pp. 2351-2378, 2009.
- [119] N. Domun, H. Hadavinia, T. Zhang, G. H. Liaghat, S. Vahid, K. Paton, C. Spacie and T. Sainsbury, "Improving the fracture toughness properties of epoxy using graphene nanoplatelets at low filler content," *Nanocomposites*, vol. 3, no. 3, pp. 85-96, 2017.

- [120] V. Georgakilas, M. Otyepka, A. B. Bourlinos, V. Chandra, N. Kim, K. C. Kemp, P. Hobza, R. Zboril and K. S. Kim, "Functionalization of Graphene: Covalent and Non-Covalent Approaches, Derivatives and Applications," *Chemical Reviews*, vol. 112, no. 11, pp. 6156-6214, 2012.
- [121] J. Park and M. Yan, "Covalent functionalization of graphene with reactive intermediates," *Accounts of Chemical Research*, vol. 46, no. 1, pp. 181-189, 2013.
- [122] A. Sinitskii, A. Dimiev, D. A. Corley, A. A. Fursina, D. V. Kosynkin and J. M. Tour, "Kinetics of Diazonium Functionalization of Chemically Converted Graphene Nanoribbons," *ACS Nano*, vol. 4, no. 4, pp. 1949-1954, 2010.
- [123] W. Zan, "Chemical functionalization of graphene by carbene cycloaddition: A density functional theory study," *Applied Surface Science*, vol. 311, pp. 377-383, 2014.
- [124] T. A. Strom, E. P. Dillon, C. E. Hamilton and A. R. Barron, "Nitrene addition to exfoliated graphene: a one-step route to highly functionalized graphene," *Chemical Communications*, vol. 46, no. 23, p. 4097, 2010.
- [125] S. Vadukumpully, J. Gupta, Y. Zhang, G. Q. Xu and S. Valiyaveetil, "Functionalization of surfactant wrapped graphenenanosheets with alkylazides for enhanced dispersibility," *Nanoscale*, vol. 3, no. 1, pp. 303-308, 2011.
- [126] M. Jung de Andrade, M. D. Lima, L. Stein, C. Pérez and S. Roth, "Single-walled carbon nanotube silica composites obtained by an inorganic sol-gel route," *physica status solidi (b)*, vol. 244, no. 11, pp. 4218-4222, 2007.
- [127] A. Lopez, A. Rico, J. Rodriguez and J. Rams, "Tough ceramic coatings: Carbon nanotube reinforced silica sol-gel," *Applied Surface Science*, vol. 256, no. 21, pp. 6375-6384, 2010.